EXPERIMENTAL PHOTOELASTIC STRAIN MEASUREMENTS AND
NUMERICAL SIMULATIONS ON MULTI-MATERIAL Pi-/T- JOINTS

By

Ryan Khawarizmi

A THESIS

Submitted to
Michigan State University
in partial fulfillment of the requirements
for the degree of

Mechanical Engineering – Master of Science

2018

ABSTRACT

EXPERIMENTAL PHOTOELASTIC STRAIN MEASUREMENTS AND
NUMERICAL SIMULATIONS ON MULTI-MATERIAL Pi-/T- JOINTS

By

Ryan Khawarizmi

An adhesively bonded Pi-/T-joint is a common 'out-of-plane' structural joint that connects a vertical (web) and a horizontal (base) load bearing substrates using an adhesive and a 3D-braided π (pi) preform. The stress-transfer between the substrates and the preform occurs through the adhesive bond-line via complex mechanisms that are governed by the loading condition and material properties of the substrates and the adhesive. Resistance strain gages and fiber optic sensors can only provide local/single-point measurement. Moreover, embedding them in the adhesive bond-line is impractical as they act as stress-concentrators and sites for the onset of failure. Optical techniques, especially the photoelasticity coating method, enables the full-field visualization of stress/strain fields.

In this work, the Pi-/T-joints were made with aluminum substrates (both web and base) and a carbon fiber pi-preform using SC-15 resin as an adhesive. The joints were manufactured using the liquid resin transfer molding technique. The photoelasticity coating method was used to visualize and measure plane strains and stress directly on the joint using polarized light. The joints were experimentally tested in 'out-of-plane' (web pull-out) configuration until failure, and the isochromatic photoelasticity fringes or strain field images from the surface of the specimen were recorded. Force-displacement data were also characterized. Numerical models were developed using commercially available software ABAQUS®. Results show reasonably good agreement between the strain maps from photoelasticity and numerical simulations for similar load levels. Improvements in technique and modeling are suggested in order to improve agreement and to gain added insight into the complex behavior of these joints.

To my parents, Yandra and Titi
and my wife, Astri Briliyanti

ACKNOWLEDGMENTS

July 2018

Ryan Khawarizmi

TABLE OF CONTENTS

LIST OF TABLES

LIST OF FIGURES

x

Chapter 1 Introduction

1.1 Background

Structural Joining of dissimilar materials, specifically joining metals to fiber reinforced polymer (FRP) composites is of immediate interest to automotive industries to reduce weight and carbon-emissions while increasing fuel efficiency. While considerable work on the study of in-plane (lap-shear) behavior of joints exist, similar work on out-of-plane (T-joints) is relatively limited. T-joints are extensively used in automotive, aerospace and marine structures. If the T-joint consists of a 3D woven preform (shaped in the form of a Greek letter 'π'), to connect the horizontal and vertical members, then such a joint is referred to as Pi-joint. The strength of Pi-/T-joints lies in its ability to distribute the load symmetrically from the vertical part (web/rib/bulkhead) to its horizontal part (base/flange/skin) and vice-versa through the bonded Pi-preform without using mechanical fasteners. Traditional T-joints use mechanical fasteners that act as locations of stress-concentrations on the bolted parts thereby affecting its strength. In general, usage of fasteners adds weight, increases cost, and production time [1]

Various configurations of multi-material Pi/T-joints have been studied to understand its behavior, advantages and its limitations. Kesavan [2] studied large-sized composite T-joints made with composite overlaminate and used resistance strain-gages to study their behaviors. Tserpes [3] studied Non-Crimp Fabric (NCF) based Pi/T-joints using pull-out tests, T-shear, T-bending, and T-tension. Sebastian, *et. al* [4] studied composite Pi-Joints made with a carbon fiber preform and used Digital Image Correlation (DIC) to validate their numerical models. These studies used Pi/T-joints made out of similar substrates, namely glass fiber reinforced polymer composites (GFRP). To the best of the author's knowledge, metal-to-composite Pi-/T-joints have not been reported elsewhere and is considered as one of the unique features of this work.

Another area that has not been fully explored in multi-material Pi/T-joints studies is the analysis of the whole-field stress-/strain- distribution. In order to build validated numerical models of these novel joints, experimental techniques that can provide such measurements are needed. One of the optical techniques to conduct whole field stress measurements is through reflection photoelasticity. "Reflection photoelasticity", also called the "photoelasticity coating method" is a classical technique that uses polarized light and a birefringent coating to measure stress distribution on the surface of an opaque structure. The birefringent coating is a type of material that doubly refracts polarized light when it is loaded. The reflected light beams from the coating, when passed through another polarizer, then form a continuous fringe pattern, apparently superimposed on an image of the structure, which is related to its strain distribution. As an example, **Figure 1-1** shows a tramsmission (not reflection) photoelasticity fringe pattern from a transparent polycarbonate block subjected to 3-point bending. In this image, the fringe patterns are divided into two parts: the upper part shows the compression stress due to bending, while the lower part shows the tensile stress.

Figure 1-1 Isochromatic fringe photoelasticity pattern on a polycarbonate block in a 3-point bending loading

Photoelasticity coating method has been employed to study stress/strain-fields on various structures. Alvarez [5] used it for bolted steel T-joint analysis. Similarly, De Lima [6] applied the method for analyzing stress distribution on a structural minor axis steel joint. Also, Fritz [7] employed the method back in 1967 to investigate the stress distribution in wood planks. Hence,

the use of the photoelasticity coating method has been broad and common, but is yet to be utilized in a multi-material Pi/T-joint study.

The application of reflection photoelasticity method on a multi-material Pi/T-joint presents an unique opportunity to reestablish a classical technique on a novel joint. In conjunction, numerical models that can be validated with experimentally measured stress-fields will also be studied.

1.2 Problem Definition and Objectives

In this research, the scope of the study is limited to **Pi-joints composed of Aluminum substrates and Carbon fiber pi-preform.** These multi-material Pi/T-joints further will be defined as aluminum pi-joints for brevity purposes. There are four reasons for choosing the configuration:

1. Joining Aluminum to FRPs is considered as one of the significant gaps in incorporating aluminum materials for lightweighting, based on the report of US Department of Energy which is summarized in **Table 1-1**.

2. Aluminum is widely used in the automotive industry but are joined using conventional techniques such as as mechanical fasteners or welding. This study aims at showing the potential of bonded multi-material joints as an alternative to existing practices.

3. On the other hand, a carbon fiber preform has strong material properties, structural efficiency (strength to weight ratio), and is easy to assemble. Theoretically, the joining of an aluminum substrate to a composite preform results in a strong joint with reduced weight and cost. As an example, , a carbon fiber composite preform application into wind blade manufacturing reduces cost by 14% due to fewer materials needed (fasteners and parts) and fewer assembly steps [8]

4. **Table 1-1** also details existing gaps for carbon fiber composite application, namely that the design methods, and predictive modeling are inadequate. This is because carbon fiber

material properties are anisotropic. A result is that composite structures need to be over-designed, thereby sacrificing the goal of reducing weight because of ignorance. Therefore, developing an experimentally validated model of Aluminum Pi-joints having a composite preform aims at addressing this issue as well.

Table 1-1. Key technical material gaps for light-weight vehicles, adapted from [9]

Structural Materials	Weight Reduction Potential	Three Most Significant Technical Gaps Impeding Widespread Implementation		
Carbon Fiber Composites	50%-70%	Lack of low-cost precursors and energy efficient conversion processes for carbon fiber	Design methods and predictive modeling capabilities are inadequate	Lack of high-volume manufacturing methods amenable to non-epoxy resin systems
Magnesium	30%-70%	Cost-effective, environmentally friendly process for magnesium production does not exist	Current alloys exhibit poor corrosion properties and insufficient ductility for crash protection and manufacturability	Models for predicting properties and behavior of components are not available
Aluminum	30%-60%	Processes for joining AL alloys to dissimilar materials and welding of 7000 series Al are inadequate	Modeling, simulation, and design tools are inadequate for optimization	Processing techniques for high-performance castings are unreliable

The specific objectives of this study will be:

- To experimentally evaluate the out-of-plane behavior of an Aluminum Pi-joint using the photoelasticity coating method to obtain whole-field strain-fields, and
- To compare the results of experimental testing with numerical simulations.

Aluminum Pi-joints in this study were subjected to web pull-out / out-of-plane configurations and constrained with simple support until failure, as shown in **Figure 1-2**. The aim was to test the adhesive bond between the aluminum substrate and the composite preform and to observe the onset and propagation of failure. During this quasi-static test, force-displacement data were recorded

while the photoelasticity strain field fringe patterns were observed until the elastic limit of the joint was reached.
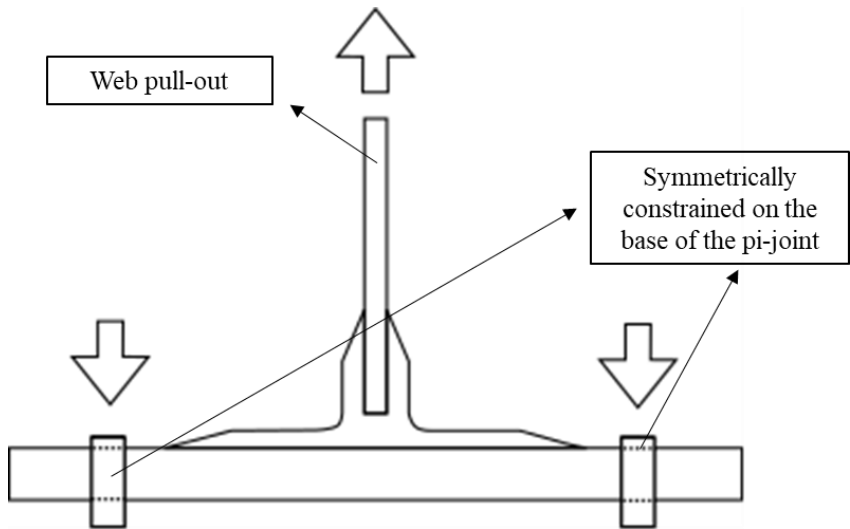
Figure 1-2. Web pull-out schematic of the Aluminum pi-joint

Three cases of aluminum pi-joints were studied to improve the validation of the numerical model. The first case was the control/baseline study, i.e., a pristine/no-defect aluminum pi-joint, while the other two cases had deliberately embedded delaminations to initiate failure. Embedded delaminations represent flaws that might occur during manufacture, hence are used to compare their effects on structural integrity relative to the control case. In summary, a schematic of the approach adopted in this work presented in **Figure 1-3.**
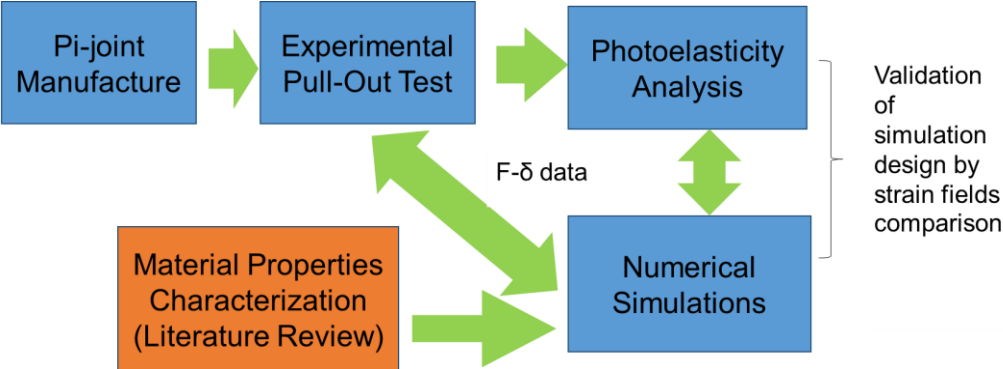
Figure 1-3. Flowchart of research approach

In conjunction with the thesis objectives, the following questions are investigated:

1. What is the failure mechanism of the Aluminum pi-joints?

2. How embedded delamination affects the structural behavior of the Aluminum pi-joint?

3. Is there any significant stress distribution difference between the pristine and defect-embedded pi-joints?

4. How accurate can the photoelasticity coating method measure stress distribution on the Aluminum pi-joints and can it predict failure before it happens?

5. What are the approximations needed to build the numerical simulation and is it comparable to actual experiments results?

1.3 Thesis Organization

This thesis is organized into eight chapters. In addition to the introduction and problem definition, a literature review was carried out and reported in Chapter 2, that includes : various pi-joints configurations and tests, photoelasticity fundamentals and applications, and finite element modeling. Chapter 3 details the manufacturing of the pi-joint specimens and how the photoelasticity coating is applied. Chapter 4 presents the experimental pull-out test configuration and isochromatic fringe recording. Chapter 5 narrates the numerical simulation procedures carried out in commercial FEA software ABAQUS© and the assumptions used in creating them. Chapter 6 presents the observations and discusses the data recorded from experimental tests and numerical simulation results. Finally, Chapter 7 provides conclusions, recommendations, and possible future directions of this work

Chapter 2 Literature Review

2.1 Pi-/T Joints Configurations and Testing

In this section, a brief reviews of literature on Pi-/T-joints relevant to this work are presented.

2.1.1 Composite T-joints

Kesavan [2] and Li [10] studied fracture behavior and damage detection of a composite T-joints. Glass fiber reinforced polymer (GPRP) laminates were used to manufacture the composite T-joints. GFRP was chosen due to its high strength to weight ratio and corrosion resistance. The 700 mm-wide composite T-joints were designed as a model of a marine structure and composed of the bulkhead, hull, filler, and overlaminates as shown schematically in **Figure 2-1**.
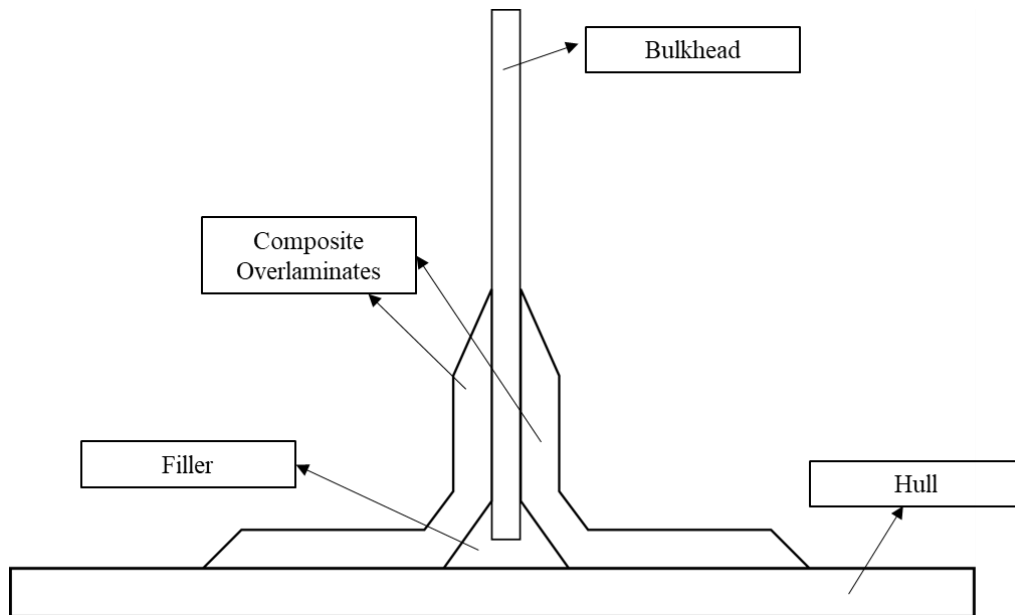
Figure 2-1. Schematics of composite marine T-joint configuration, adapted from Kesavan [2]

In this work, the bulkhead and the hull were joined using composite overlaminates which is mainly composed of layers of GFRP and layers of chopped strand mats on the interface. To increase bonding of the components, the filler was manufactured using resin infused with glass particles in the gaps between bulkhead, hull, and overlaminates. Overlaminate layers then were bonded into

the side surface of the marine T-joint using wet hand lay-up method. During the assembly process, delaminations made from thin strip of Teflon ® with the thickness of 60 µm and the length of 30, 60, and 90 mm were embedded throughout the structure with different locations.

Composite marine T-joints then were attached with resistance strain gage (RSG) on the location which deliberately induced cracks were embedded. These sensors would measure the impact of delamination on the joint's strength. Next, the T-joints were loaded in a tensile testing machine from initial load to 5 kN with 0.5 kN increments, and later loaded into failure. The strain data from the sensors were recorded and analyzed. Then, tests were repeated for other cases of delamination that had different locations and length.

Data gathered from experimental strain gages measurements were then relayed into an Artificial Neural Network (ANN). ANN is a series of processors that records and communicates the data of the delamination size and locations from the pull-out test. The network was connected into a numerical simulation of the composite T-joint on MSC/Patran ® with 8 strain gages located along the overlaminates. A similar model of composite T-joint then was built with different locations and sizes of delamination to detect and predict delamination throughout the model. The study concludes that the ANN trained with experimental pull-out data from strain gages can detect the location and the extent of damage on a numerical model of a composite T-joint with the accuracy of 98.4 %.

In another study by Dulieu-Smith, *et. al*. [11], a GFRP composite T-joint was tested using thermoelastic stress analysis (TSA) method. The measurement was based on a phenomenon which material yields a small temperature change during elastic cyclic stress, and the change is proportional to the sum of the principal stress changes. SPATE (Stress Pattern Analysis by the

measurement of Thermal Emissions) is the standard equipment to conduct TSA. The analysis from TSA was then compared with numerical simulation from ANSYS ®

The configuration of the composite T-joint in this research is shown in **Figure 2-2.** The substrates (web and flange) were 15 mm thick and composed of 17 layers of glass fiber woven roving composite cured in Scott Bader Crystic 489 polyester resin. The fillet was formed using a resin that was infused during manufacturing to achieve the desired shape. Overlaminates / boundary angles were constructed to support the connection between web and flange. A mix of layered chopped strand mats and glass fiber was cured with polyester and urethane acrylate resin to form a nominal overlaminate thickness of 15 mm. Once successfully cured, 100 mm-thick specimens were cut from the assembly.
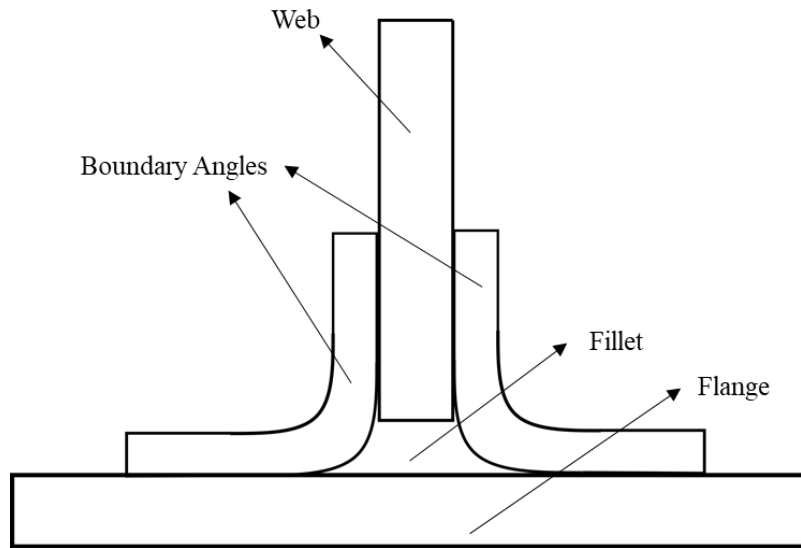
Figure 2-2. Composite T-joint schematics, adapted from Dulieu-Smith *et. al*. [11]

The study successfully obtained full-field stress pattern on a complex joint using TSA. Joint behavior was characterized by utilizing the infrared camera to measure really small temperature changes on the tested specimen. Load-displacement and stress distribution were both in reasonably

9

good agreement between experiment and numerical simulation. The difficulties of TSA relies on calibrating materials of the joint to yield an accurate stress data during the test.

2.1.2 Non-Crimp Fabric (NCF) Composite Pi-joints

Tserpes, Ruzek, and Pantelakis [3] studied the strength of non-crimp fabric (NCF) composite pi-joints in four types of loading condition. NCF is a multi-ply multi-axial fabric material which was stitched together with flexible configurations. In this study, the substrates and pi joining elements were made with quasi-isotropic HTS/RTM6 NCF quad layers using hand layup methods. The elements were joined by a mix of adhesive paste EA9395 and EA 9396 with a mean thickness of 0.5 mm for the insert-pi interface. On the other hand, the skin-pi interface bonding relies on interlaminar adhesion from the manufacturing process. Schematics of the joint from this study is shown in **Figure 2-3**.
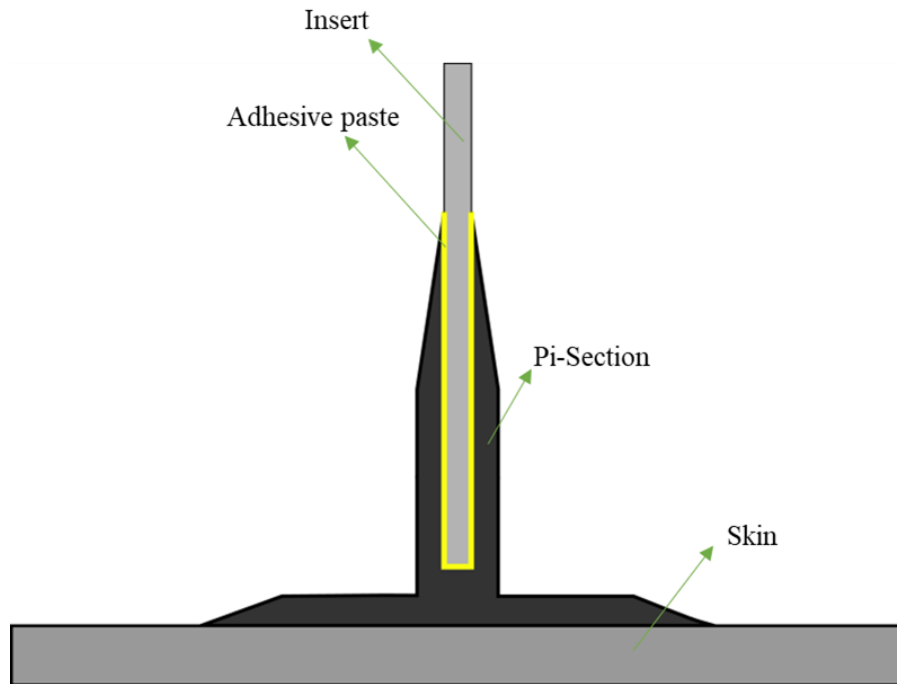
Figure 2-3. Schematics of composite NCF Pi-joints adapted from Tserpes, *et. al* [3].

Composite NCF joints were subjected to T-pull, T-shear, T-bending, and T-tension load. For each load case, at least three specimens were tested. All test except T-tension were conducted using a Schenk machine with a load capacity of 250 kN whereas the T-tension was conducted with an MTS-810 machine with the same 250 kN load capacity. Load-displacement curves were characterized for each test and photographs of specimens before and after loading were captured. In addition, a numerical simulation was built using ANSYS® to support experimental results and provide better insight on damage details.

The results from NCF Pi-joints tests are summarized in **Table 2-1**. For the T-pull test, the average load was 6.81 kN with the mode of failure of delamination of skin from pi-element or bending of the skin itself. Bond line quality of the insert-pi interface was undisturbed for each test indicating that the load was successfully transferred throughout the structure. Simulations show that inter-laminar fracture initiated at the edge of the pi base/skin interface and then propagated inwards. This was caused by large normal stresses that maximized on the edge of pi-element. The T-shear tests caused the insert to be completely detached from the pi-element walls due to shear. The shear load averaged around 70 kN. De-bonding was due to the interaction of a combination of secondary failure mechanisms including extensive ply cracks, fracture at the boundary layer, and adhesive fracture. The T-bending tests also resulted in complete de-bonding of the insert with pi-walls from large tensile normal stress between them. The average T-bending load was 2.68 kN. Lastly, the T-tension experiment was conducted to measure the response of skin-pi interface under tensile loading. It is similar in load setup to a mode-1 crack length test. Initially, there was a crack initiation on the skin-pi interface due to mismatch of inter-laminar strength. The main failure mode in this test was skin fracture due to tensile stress on the skin fibers. There was no bond-line failure

observed in these tests as there was no direct load applied. Average load reported for T-tension was 106 kN.

Table 2-1. Summary of results from Composite NCF Pi-joint tests, adapted from Tserpes, *et. al* [3].

Load Case	Primary failure mechanism	Failed part
T-pull	Interlaminar cracking / skin bending	Pi/skin interface, skin
T-shear	Debonding (shearing)	Bondline
T-bending	Debonding (fracture)	Bondline
T-tension	Interlaminar cracking / skin fracture	Pi/skin interface, skin

2.1.3 Pi-preform Composite Joints

Dr. John D Russel [12] from the Air Force Research Laboratory (AFRL) reports that Pi-preform joining has three advantages, namely structural efficiency, greater strength than double lap shear joints, and reduced assembly times. The study was similarly adapted in industrial cases, namely the NASA crew module [13] and commercial wind blades [8].

Sebastian *et. al.*, [4] studied the behavior of a composite pi-preform joint using Digital Image Correlation (DIC). DIC is a non-destructive evaluation method that uses random speckle pattern sprayed on the joint's surface to observe the whole-field stress displacement distribution. DIC equipment consists of a camera and a computer to calculate the displacement of each point. The displacement map is then differentiated to obtain the strain distribution. With careful work, strain sensitivities on the order of a few hundred micro-strain can be achieved. In addition to the experimental test, numerical simulation was devised using ABAQUS ® to compare pull-out behavior.

In this study [4], GFRP substrates were connected using a carbon fiber reinforced pi-preform. Preform joining is a novel and simple method of manufacture, in comparison of previous composite Pi/T-joint studies which used overlaminates or pi-layups. Substrates and preform were assembled inside an aluminum mold to achieve the specified joint dimensions. SC-15 resin adhesive was infused to bond all the elements using Vacuum Assisted Resin Transfer Molding (VARTM). Steel wires of 0.127 mm diameter were located strategically to ensure bond-line thickness. Then, composite pi-joints were tested on a servo-hydraulic test machine with a loading rate of 1 mm/min until failure.

Results from the DIC measurement and numerical simulation were reported to show good agreements shown in **Figure 2-6**. This image shows strain maps from DIC and numerical simulation during a 3 kN pull-out test. The value of peak pull-out load between experiments and model agreed very well (~10% difference). Thus, it was reported that such validated simulations have good potential as a design tool for further composite preform joints.
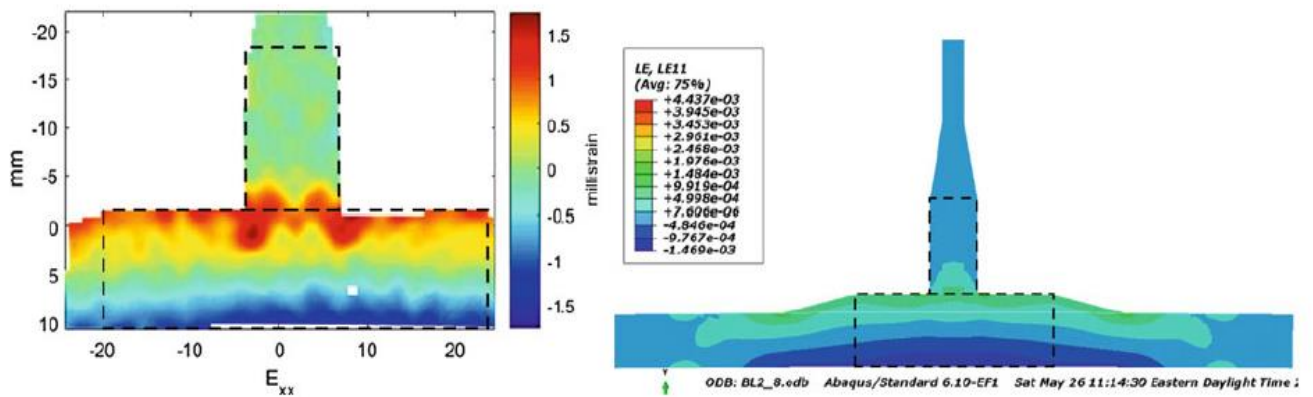
Figure 2-4. Comparison of Strain in the x-direction from DIC (left) with E11 data from simulation (right) [4]

2.1.4 Concluding Remarks

The literature cited above can be summarized in three points:

- There have been various studies of joining composite to substrates in the form of out-of-plane T-joints. Common methods of joining included overlaminates and filler, transverse stitching, hand-layup pi, and pi-preform. Pi-preform holds a competitive advantage compared to other joining methods due to its modular manufacturing and consistent properties. However, studies on pi-preform reinforcement joining are relatively limited.

- Generally, metal substrates have not been used for composite T-joint studies. This deficiency evolves from the difficulties of joining metal to composites. Despite the difficulties, joining dissimilar materials of metals to composites remains an important issue for study.

- T-joint experimental characterization relies on machine load-displacement measurement and common point-by-point measurement, such as resistance strain gages. DIC and TSA have been used in some studies to characterize the behavior of these complex out-of-plane T-joints. To the best of author's knowledge, optical methods such as photoelasticity have not been employed to study composite Pi/T-joints. Photoelasticity is discussed further in the next section.

2.2 Photoelasticity

Photoelasticity was a classic physical phenomenon first observed by Sir David Brewster back in 1815 [14]. He discovered that light becomes doubly refracted inside a loaded Iceland Spar crystal (Ca_2CO_2). This observation was later applied in the study of engineering problems during the early part of the 20th century by Coker and Filon [15], M.M Frocht [16], and many others. Later, a photoelasticity coating method or reflection photoelasticity was devised by Zandman [17] [18], and has been widely used in a host of applications. For example, the photoelasticity coating method was applied by Fritz [7] and Meisenhamer [19] during the 1970s to study wood and soil characterization, respectively. Recently, the use of traditional photoelasticity and reflection photoelasticity has not been quite popular as it used to be. Some notable works in photoelasticity in recent years were by Alvarez in the study of a T-stub flange joining using bolt [5], by De Lima in the characterization of steel structure [6], by Driscoll who explored shear stress during running [20]. Many writings, such as those by Cloud [21], Ramesh [22], Patterson [23] have broadly explained the photoelasticity fundamentals and applications with clarity. The theory underlying photoelasticity, basic principles, applications, and limitations are explained briefly in the following sections.

2.2.1 Theory

Light can be described as an electromagnetic wave that vibrates in all direction and differs in its wavelength or frequency. White light such as from the sun or incandescent household lamp is a type of light that is composed of a broad spectrum of wavelengths. In contrast, a singular wavelength or frequency is called a monochromatic light. When a white light source enters a polarizing filter or polarizer, light vibrations becomes constrained into a single plane parallel to

the polarizing axis. The polarizer absorbs the electromagnetic energy vibrating in all other planes. Thus, the resulting radiation is called polarized light or, specifically, plane polarized light.

The speed of light in a vacuum such as outer space is constant at approximately $c = 3x10^8$ m/s. However, when light travels through a transparent material, it slows down. The ratio between the speed of light in vacuum and the decelerated speed of light in materials is defined as the index of refraction. The value of the refraction index is always greater than unity for known matarials, and it is isotropic in a homogeneous material. Nevertheless, the refractive index in some materiasl x is anisotropic due to its natural molecular structure or because temporary loading distorts the material at the atomic level.

The interaction between light and materials with optical anisotropy is unique. Light waves are refracted more than once because of the multiple refraction indices in the material. The phenomenon is known as birefringence. Interaction of polarized light with materials that exhibit birefringence (birefringent materials) form the foundation of photoelasticity. An illustration of the effect of birefringence on a plane polarized wave is given in **Figure 2-6** [24]
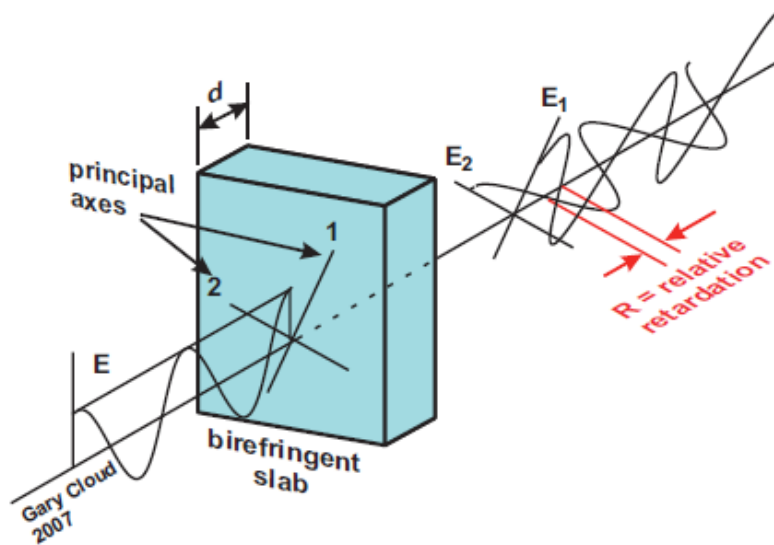
Figure 2-5. Birefringence illustration by Dr. Gary Cloud [24]

From **Figure 2-6,** the vertically polarized light (E) enters the birefringent slab with the thickness (d). E is refracted into two different light vectors, E_1, and E_2 that are orthogonal. The orientation of each vector is parallel with one of the principal axes of the birefringent slab. In addition, each principal axis has its own refraction index. Hence, one of the light vectors will be 'out-of-phase' with respect to the other vector when they exit the slab. The phase difference between these two waves is defined as the relative retardation (R).

Mathematically, relative retardation is defined as follows:

- Assume that the speed of light in our atmosphere is not significantly different from the speed of light in a vacuum. Absolute retardations in units of length for each of the light waves defined by E_1 and E_2 are defined as R_1 and R_2. These retardations which is the multiplication of the light speed (c) with the relative time for each wave to travel the birefringent slab (d/V). Each of the absolute retardations can be calculated as the difference

17

between the distance the wave would travel in the time it takes to transit the slab (i.e. thickness/velocity) and the actual thickness of the slab, as follows:

$$R_1 = c\left(\frac{d}{V_1}\right) - d \text{ and } R_2 = c\left(\frac{d}{V_2}\right) - d \tag{2.1}$$

- Recall that the index of refraction n is the ratio of the speed of light in a vacuum to the decelerated speed of light in the medium. Also, relative retardation (R) is defined as the difference between R_1 and R_2, giving,.

$$R = c\left(\frac{d}{V_1} - \frac{d}{V_2}\right) = (n_1 - n_2)d \tag{2.2}$$

Thus,

$$R = (n_1 - n_2)d \tag{2.3}$$

- It was established by Brewster that the change of refractive indices in a birefringent material is proportional to the changes of principal stress. The relation is called Brewster's Law or the Stress-Optic Law.

$$n_1 - n_2 = K_\sigma (\sigma_1 - \sigma_2) \tag{2.4}$$

Where K_σ is the stress-optic coefficient which is related to the properties of the materials and σ_1 and σ_2 are the principal stresses. Furthermore, the principal stress axis are coincident with the principal axes of refractive index.

- From (2.3) and (2.4), relative retardation can be written as:

$$R = K_\sigma (\sigma_1 - \sigma_2) d \tag{2.5}$$

Equation (2.5) is the mathematical definition of relative retardation which is the function of material properties, dimensions, and principal stress condition. Thus, the measurement of the

relative retardation from a birefringent slab enables the measurement of stress, as long as the properties and dimensions of materials are known. The relative retardation relates linearly to the state of stress during material loading in the linear elastic regime. This correspondence between stress state and relative retardation forms the foundations of photoelasticity.

2.2.2 Plane Polariscope

The equipment used to measure relative retardation in a birefringent material is called the polariscope. A polariscope consists of a light source, a polarizer, a birefringent slab, another polarizer called an analyzer, and a sensor. A polariscope can measure the birefringence of materials due to the interference of light waves that the sensor receives. Details of one of many polariscope configurations are shown in **Figure 2-7**. This configuration is further defined as plane polariscope because the light travels in one plane of direction (y-z) from the first polarizer to the specimen.

From **Figure 2-7**, it can be seen that the plane polariscope is sort of an expansion of **Figure 2-6**. Both of the light vectors from the transparent slab are passed through an analyzer, which is another polarizing filter. In this configuration, the analyzer was set to have a perpendicular angle to the polarizer. If there was no birefringent slab in place, no light passes the analyzer. Hence, this is called the dark-field plane polariscope.
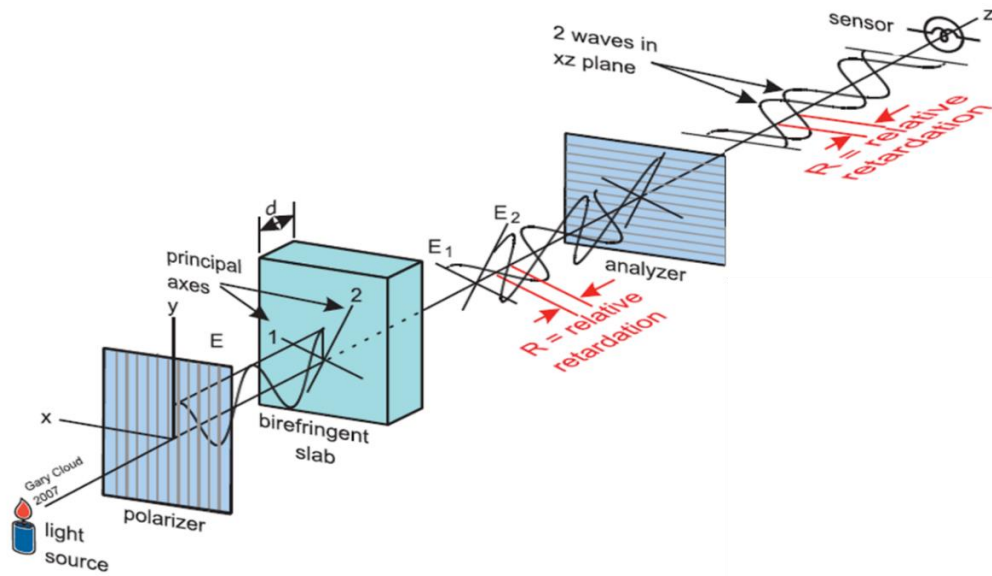
Figure 2-6. Dark-field plane polariscope, Drawing used courtesy of Dr. Gary Cloud [24]

Once light vectors E_1 and E_2 enter the analyzer, it becomes a combination of two coherent light waves lying in a plane that maintain the relative retardation. The relative retardation is the item of interest, however, no sensors, including the human eye or a camera is sensitive to retardations. So, interference between the waves is used to convert retardation difference to something that can be detected, namely irradiance (intensity0. The light waves interfere to produce a resultant intensity that depends on the relative retardation and their respective individual intensities. The intensity is captured by a sensor, which could be a camera or a human eye. Combining the waves, each of which has been retarded according to the equations given above yields the amplitude of the resulting wave vector [E_s] for a plane polariscope [24], as follows:

$$E_s = A \sin\frac{\pi R}{\lambda} \sin 2\phi \left\{ \sin\frac{2\pi}{\lambda}\left[z - vt - \left(\frac{R_1 + R_2}{2}\right)\right]\right\} \qquad (2.6)$$

The wave equation contains an amplitude part and a wave part. Since the sensor can only detect the amplitude, we focus on that part of the interference result:

20

$$E_s = A \sin \frac{\pi R}{\lambda} \sin 2\phi \qquad\qquad (2.7)$$

Equation 2.7 contains the amplitude of the light source (A), relative retardation (R), light source wavelength (λ), and the angle between the polarizer and the first principal stress axis (ϕ). This equation gives three condition where the resulting amplitude is equal to zero, meaning the intensity level is dark. First is the trivial case where the amplitude's source is zero. Second, is when the value of $\sin (\pi R/\lambda)$ is equal to zero. The third is when $\sin 2\phi$ equals zero. The second and the third cases of interference extinction of a light wave through a birefringent slab yields what are known as isochromatic and isoclinic fringes.

2.2.3 Isoclinics and Isochromatics

An isoclinic is defined as the set of points that has the constant inclination of the principal axes of refractive index, therefore of principal stresses. An isochromatic, on the other hand, is the set of points that have the same colors, therefore the same relative retardations. These two type of lines appear on a birefringent slab which viewed in a polariscope. These two patterns are the main interest in photoelasticity.

Mathematically, the isoclinic pattern on a dark-field plane polariscope happens when:

$$\sin 2\phi = 0 \text{ , then } \phi = 0 \text{ or } \pi/2 \qquad\qquad (2.8)$$

Meaning when there is no angle difference between the material principal stress axis and the polarizer axis, no light will be detected by the sensor. Remember, in this case, the polarizer and analyzer are mutually perpendicular. Hence, the parallelism of the principal axes of stress and the principal axes of refractive index yields isoclinic lines. These lines are used to determine principal stress directions.

A zero intensity isochromatic, on the other hand, occurs when:

$$\sin \frac{\pi R}{\lambda} = 0 \qquad\qquad (2.9)$$

This situation occurs when:

$$\frac{\pi R}{\lambda} = 0, \pi, 2\pi, \ldots \tag{2.10}$$

Hence, the relative retardation along a dark isochromatic fringe is

$$R = 0, \lambda, 2\lambda, \ldots, n\lambda \tag{2.11}$$

Recall the previous mathematical definition of relative retardation:

$$R = K_\sigma \left(\sigma_1 - \sigma_2\right) d \tag{2.5}$$

Finally we can from equations 2.5 and 2.11, assemble a new equations:

$$(\sigma_1 - \sigma_2) = 2\tau_{max} = \frac{n\lambda}{K_\sigma d} \text{ with n= 0,1,2, } \ldots \tag{2.12}$$

Equation 2.12 indicates that no light reaches the sensors when the principal stress difference is a multiple integer of the light source's wavelength divided by the birefringent material properties (stress-optic coefficient and the thickness). This relation is very useful to measure the stress in a loaded specimen. Once the order, n, of the isochromatic line is known, then the distribution of maximum shear stress is then directly obtained. However, determining the order of fringe is not an easy task.

In order to understand isoclinic and isochromatic fringes, a simple experiment was conducted using a transparent polycarbonate disk with a 6-inch diameter and 0.3-inch thickness. Polycarbonate is a known birefringent material. The disk was loaded in uniaxial compression and setup in a dark-field plane polariscope. In **Figure 2-8,** the resulting pattern from the birefringent disc is shown.

In the image, the color lines on the top and bottom disk are isochromatic fringes. This comes from the compressive load that was applied on the top and bottom of the disk. Each color indicates different levels of stress. This is going to be discussed further in another section. The large dark cross in the middle is the isoclinic fringe,which comes from the polarizer and analyzer axis that are crossed in a dark-field polariscope. This axis is coincidentally parallel with the principal stress in the specimen. This isoclinic pattern is called the 0-degree inclination of isoclinic, because the polarizer and analyzer axes are vertical and horizontal, respectively

If both the analyzer and polarizer are rotated 30 degrees with respect to the birefringent slab and remain crossed, the isoclinic pattern will change. As shown in **Figure 2-9**, the isoclinic forms two curved lines instead of a dark cross' it seems that the isoclinic pattern 'moves' as the polarizers are rotated. In contrast, the isochromatic pattern remains the same. This result demonstrates further the meaning off equation (2.7) which states that only a change of angle corresponds to light extinction if the load stays constant. In this particular example, the dark lines represent the area in which the principal stress have 30 degrees of inclination.
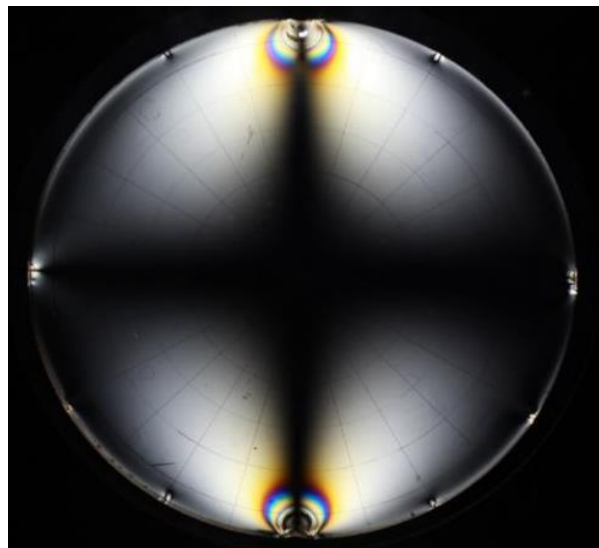
Figure 2-7. Isoclinic and Isochromatic pattern on a compressed polycarbonate disk where polarizer and analyzer in a linear polariscope are vertical and horizontal.
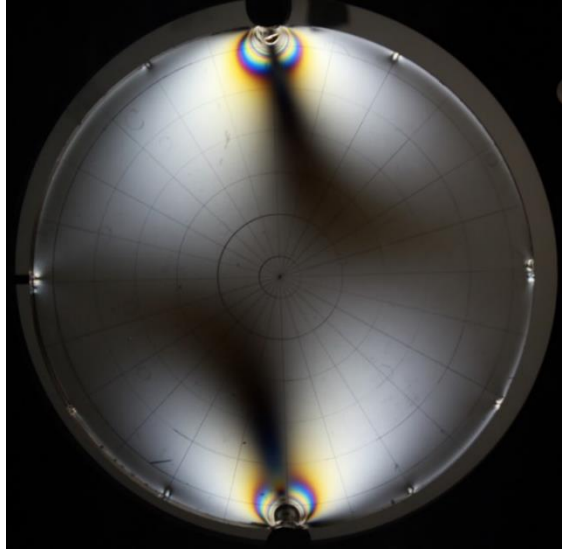
Figure 2-8. Isoclinic and Isochromatic pattern on the same specimen with polarizer and analyzer rotated 30º

In order to get the correct fringe order for the isochromatic fringe pattern, each line with the same color is numbered. However, as seen in **Figure 2-8** and **Figure 2-9**, some parts of the isochromatic are covered by the isoclinic fringes. Hence, isochromatic fringe analysis becomes disturbed by the presence of isoclinic lines. In a polariscope with monochromatic light, distinguishing isoclinic and isochromatic pattern is a huge problem, because both patterns consist of dark and light fringes. Thus, how can isochromatic patterns be separated from isoclinic fringes when performing photoelasticity studies?

A quarter wave plate is a type of birefringent slab that retards the polarized light in the amount of one-quarter of the wavelength. This causes plane polarized light to become circularly polarized light. The electric vector E for circularly polarized light traces a circular helix as it travels along the optical path. No directional information is available with circularly polarized light. Hence, the isoclinic fringes do not appear and the isochromatic fringe pattern can be easily determined by adding quarter wave plates to the polariscope, converting it to the so-called circular polariscope.

First, a quarter-wave plate is inserted between the polarizer and the loaded material, with its principal axes inclined at 45° to the polarizer axis. The second quarter-wave plate is placed between the loaded material and the analyzer, with its principal axis at 90° to the first quarter-wave plate.

Figure 2-10 illustrates the previous experiment of the compressed polycarbonate disk, but now the polariscope is implemented with quarter-waveplates properly inclined to convert it to the circular type. The only isochromatic fringe pattern appears on the top and bottom of the disk, as the isoclinic patterns were 'erased.' The clear isochromatic pattern indicates the biaxial compression of the disk. Also, numbering the fringe orders of the isochromatic pattern becomes more convenient. Hence, the stress condition can be measured more accurately.
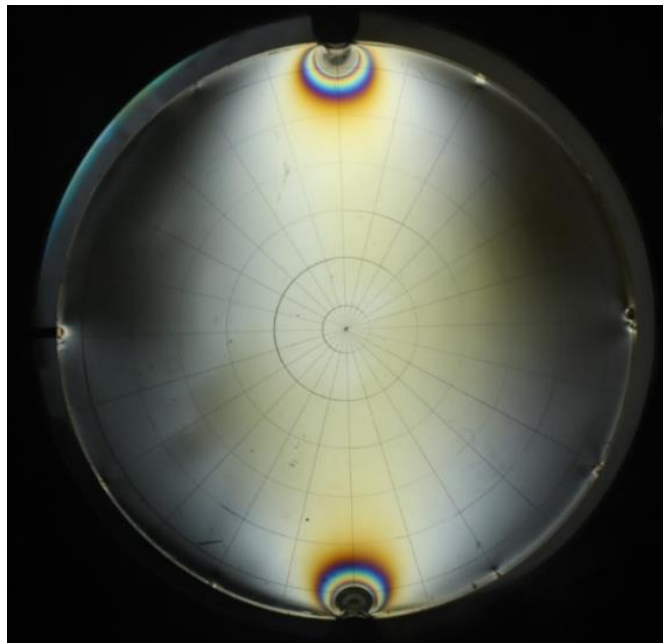
Figure 2-9. Isochromatic fringe on a compressively loaded polycarbonate disk viewed in a dark-field circular polariscope.

2.2.4 Reflection photoelasticity / Photoelasticity coating method

Another polariscope configuration available in photoelasticity is called the reflection polariscope. In this setup, the polariscope is 'folded' in the middle and consists of the same equipment as the transmission polariscope described above. Details of the setup are presented in **Figure 2-11**. This configuration enables the light source and sensor to come from roughly the same direction. Such a polariscope is used for reflection photoelasticity, also called the photoelasticity coating method, which is used to study and measure whole-field stress/strain distributions on the surface of opaque structures or non-birefringent materials.
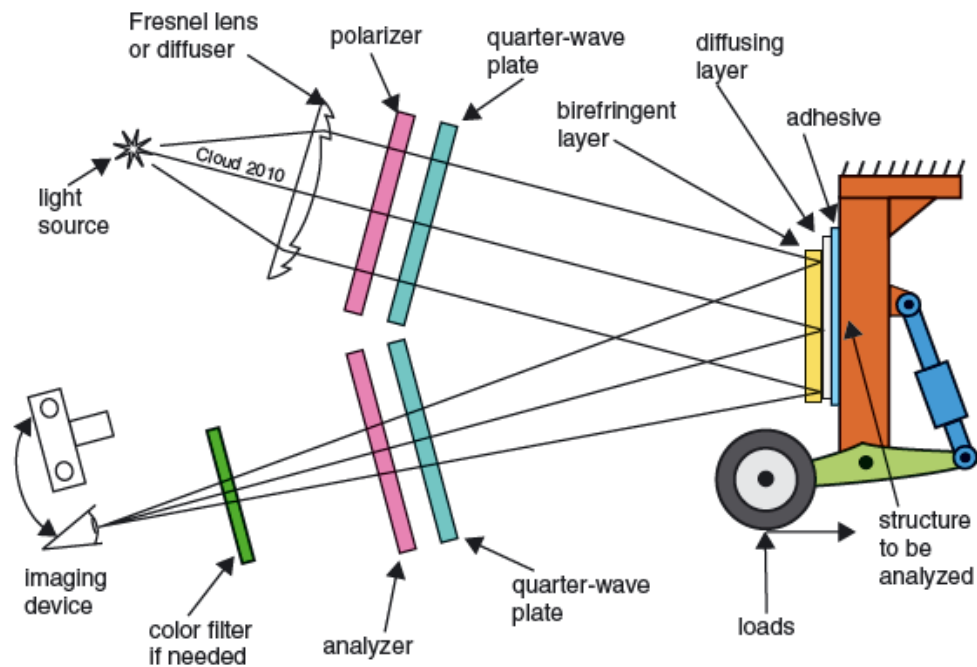
Figure 2-10. Reflection polariscope setup on a loaded airplane structure. Drawing used by courtesy of Dr. Gary L. Cloud [25]

In the reflection polariscope setup, polarized light travels twice the the birefringent coating. Thus, light travels through the distance of 2d inside the coating. The loaded structure transfers the strain directly to coating instead of the stress. Hence, an isochromatic fringe pattern emerging from this

setup relates to the principal strain difference. The relative retardation equation fromequation (2.12) transforms to:

$$(\varepsilon_1 - \varepsilon_2) \;=\; \frac{n\lambda}{2K_\varepsilon d} \tag{2.13}$$

Where K_ε is the new strain-optic coefficient, derived from appropriate calibration of the material in a known strain state:

$$K_\varepsilon = K_\sigma \left(\frac{E_c}{1 + \upsilon_c} \right) \tag{2.14}$$

E_c and υ_c respectively are the Young's modulus and the Poison's ratio of the coating. The K_ε value is usually given by the manufacturer of the birefringent coating. However, when conducting precise photoelasticity experiments, one must be able to ensure through calibration the strain-optic coefficient used.

2.2.5 Photoelasticity Coating Method applications

The photoelasticity coating method is a very powerful engineering tool that has been used in many applications. Its ability to directly measure strain from the observed isochromatic pattern is unique, intuitive, and, with appropriate technique, accurate. In this section, several examples of the photoelasticity coating method applications are presented. Experimental setups, results, and limitations are addressed in brief.

Fritz in his thesis [7], used the photoelastic coating for the stress analysis of the wood. He applied a photoelastic coating to measure the modulus of elasticity from a Douglas-Fir board and investigate stress distribution around butt joints in six-ply laminates. Since digital camera did not exist at the time, isochromatic fringe patterns were traced manually on a paper. 90% accuracy was achieved with a linear regression analysis between the photoelastic coating and strain gage data.

De Lima *et al*., [6] used a photoelasticity coating to determine structural steel column web stress and strain distribution in minor axis semi-rigid joints. PS-1 coating from Micro-measurements ® was applied around the bolted joints, and cantilever beam loading was applied to the corresponding steel I beam. A numerical simulation was devised to compare the strain distributions. Fairly good agreement was found between photoelastic strain patterns and the simulations.

Carazo *et. al*. [5] used a PS-3C photoelastic coating from Micro-measurements ® to study the location of the onset yielding of steel T-stub connected flange to flange using a steel bolt as defined by Eurocode. Experimental results were compared with predictions from numerical simulations. The photoelasticity coating methodenables a better understanding of bolted T-stub joints than the existing standard because it shows the effects or contact force, bolt interaction, and localized plastic behavior. **Figure 2-11** presents the isochromatic image of a bolted T-stub joint that undergoes plastic load and yield has occurred.

Figure 2-11. The isochromatic whole-field strain fringe pattern of bolted T-stub joints [5]

Driscoll, *et. al*. [20] utilized the photoelasticity coating method to study the interaction between a studded shoe and its surface contact during running. In this dynamic measurement, the coated surface material was subjected to impact by the running shoe. The shear stress patterns then emerged in the form of greyscale isochromatic fringes that indicate the high-stress concentrations and also stress trajectories. Image processing software was used to identify whole order fringes from the impact recording. Maximum shear stresses were measured between 0.12-0.16 MPa. The areas of which high-stress concentration occurs on the coating correlates with areas that have higher probability of foot injury.

Finally, Fernandes *et. al*., [26] used the reflection photoelasticity method to monitor stress distribution in bio-mechanical sample of dental prosthetic devices. A birefringent resin with 2 mm thickness was coated to the dental sample and stress and patterns of the loaded sample were captured using the reflection polariscope. Strain gages were employed as well to measure localized strain. Whole-field strain levels were compared with the strain gages measurements and showed high correlation (r=0.98).

2.2.6 Photoelasticity Advantages and Limitations

The photoelasticity coating method can be applied in various structures and yields quality information about strain distribution in the structure. Specifically, if used to study composite Pi/T-joints, this method has advantages over other experimental strain analysis techniques. Comparisons between the photoelasticity coating method and other existing experimental strain measurement methods are summarized in **Table 2-2.**

Table 2-2. Comparison of experimental methods for stress/strain analysis on a composite Pi-/T-joint

Methods	Comparison of experimental methods for stress/strain measurement on a composite Pi-/T-joint			
	Whole-field	Direct stress/strain	Speed	Cost
Resistance Strain Gage	-	-	-	✓
Digital Image Correlation (DIC)	✓	-	✓	-
Thermoelastic Stress Analysis (TSA)	✓	-	✓	-
Photoelasticity Coating Method	✓	✓	✓	✓

From **Table 2-2**, photoelasticity is the only method which enables a direct strain analysis as distinct from other methods that usually measure displacements that must be differentiated to obtain strain. Also, the cost for the photoelasticity coating and polariscope is relatively low compared to the specialized camera and software used in DIC and TSA. Thus, the photoelasticity coating method has a great potential for studying strain behavior in the complex pi-preform joint. However, conducting photoelasticity strain measurement always requires that the material used as the birefringent coating and the light source used be taken into account. With careful and informed technique, the measurement results from photoelasticity can be more accurate than those derived from other methods.

Chapter 3 Pi-joint Specimen Manufacturing

3.1 Manufacturing of Aluminum Pi-Joints

Aluminum pi-joints were manufactured at the Michigan State University Composite Vehicle Research Center (MSU CVRC). In general, fabrication was done by connecting Aluminum 6061 substrates with a 3-D braided tri-axial carbon fiber preform (Albany Engineered Composites, Inc) inside a specialized mold. Then, 2-part epoxy resin SC-15 (Applied Poleramics) was infused into the assembly using the Vacuum Assisted Resin Transfer Molding (VARTM) method. The resin was then cured. The result was a pi joint that was 18 inches long. The assembled joint was then sliced into 7-8 individual samples, each having 2 inch thickness, for testing. A schematic drawing of such a pi-joint specimen is presented in **Figure 3-1.**
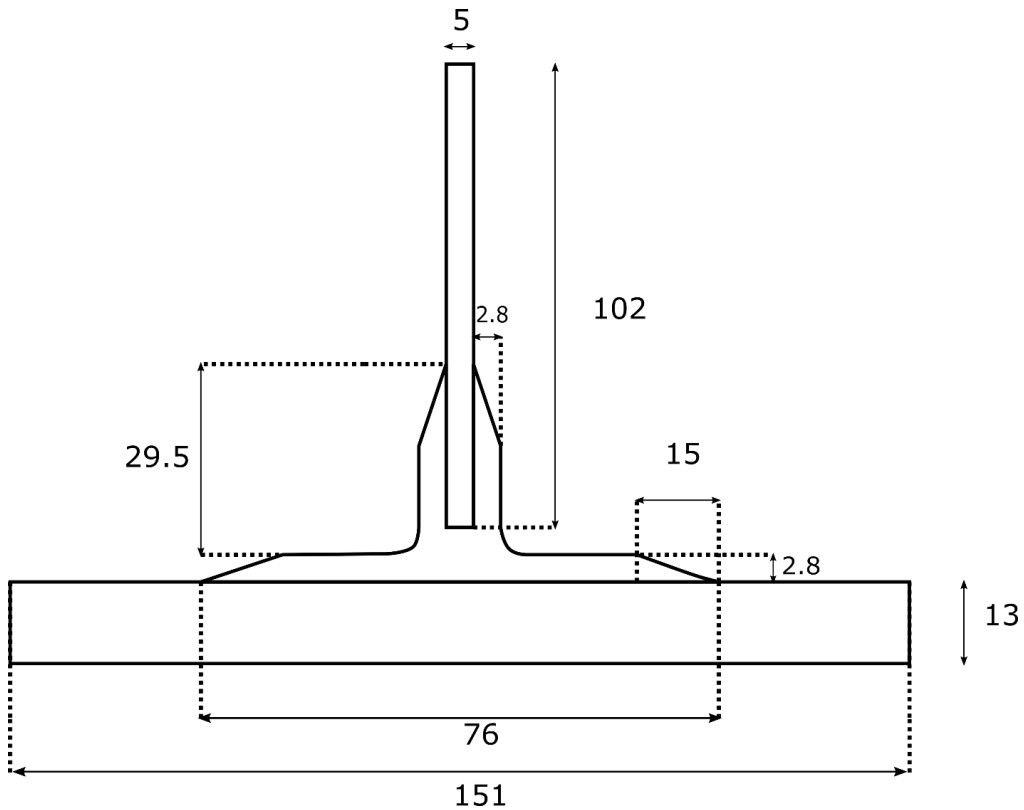
Figure 3-1. Drawing schematics of pi-joints specimens. Dimensions in mm (10^{-3} m). Not to scale.

The step-by-step process for manufacturing the aluminum pi-joints is explained below:

1. A specialized joint mold previously designed for modular assembly and fabricated from mild steel was slightly modified to produce specimens of consistent high quality

2. Aluminum 6061 plates were prepared and cut using a band saw. For the horizontal substrate or the base of the joint, the dimensions were 18"x 5.56" x 0.56". The vertical substrate (web) has dimensions of 18" x 4" x 0.2 ". After cutting to the specified dimension, both substrates were sandblasted and degreased with acetone. No other surface treatment, such as etching, was implemented. **Figure 3-2** shows the finished aluminum substrates.
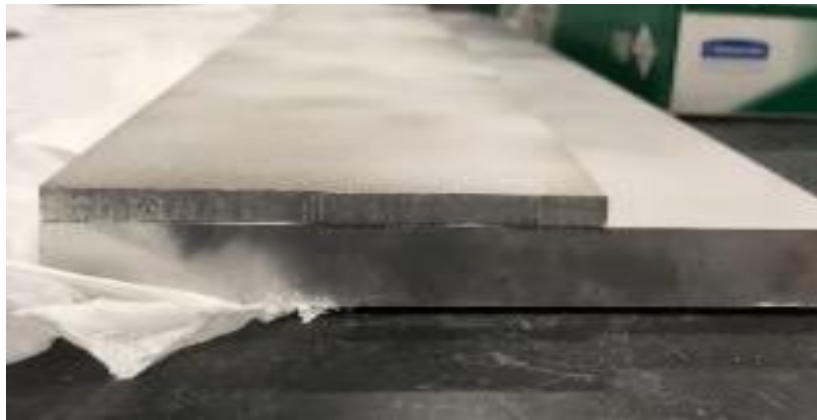
Figure 3-2. Aluminum substrates; web (top), base (below).

3. The carbon fiber braided preform 'legs' (**Figure 3-3)** were straightened from their initial flat states using the joint mold. The preform was kept inside the mold with a dummy base and web for at least 4 hours to ensure that it becomes approximately pi (π) shaped.

Figure 3-3. 3-D braided carbon fiber preform (Albany Composites, Inc.)

4. When called for, the device for creating a deliberate crack or delamination within a joint was prepared using a thin layer of Teflon. Each part of the mold was sprayed with a chemical release agent to prevent resin from sticking to the mold during manufacture and later ensure quick disassembly.

5. **Figure 3-4** illustrates the assembly of parts for manufacturing the pi-joint. Substrates, preform, and, when needed, delamination films were assembled inside the joint mold. Markings were drawn on the base of the joint at 2 inch increments to mark where the joint would be cut into individual specimens. Then, each end plate of the mold was attached with a 10 mm thick silicone sheet between the end plate and the joint assembly. The silicone sheet acted as a gasket seal to prevent vacuum loss inside the assembly. The image shows only half of the mold to display clarity.
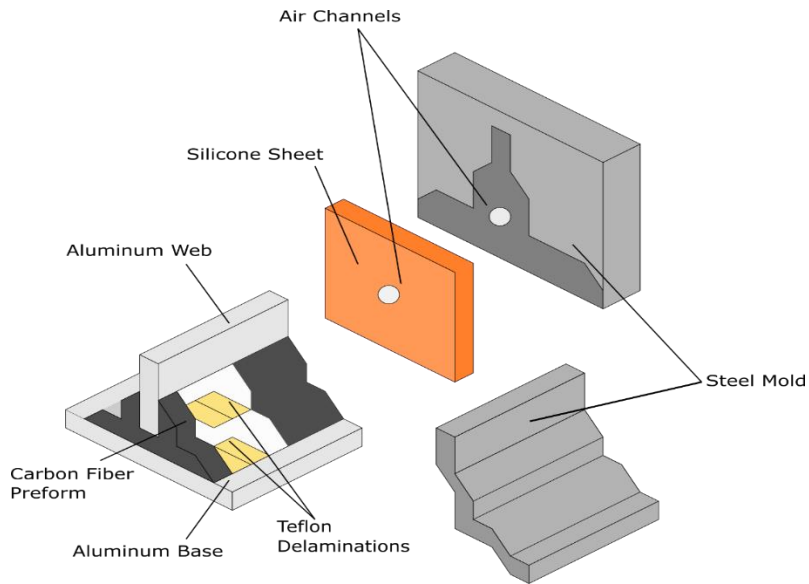
Figure 3-4. Assembly of parts in manufacturing Pi-joints

6. Sealant tape was placed around all mold seams to assure vacuum. Finally, elastic air tubes were inserted into the air channels at each end. The completed assembly for pi-joint manufacturing is presented in **Figure 3-5.**

Figure 3-5. Completed assembly for manufacturing aluminum pi-joints

7. Vacuum was created inside the assembly using an air pump. Meanwhile, inspection was done using an ultrasonic leak detector throughout the mold to ensure that there were no leaks. After reaching the desired pressure (18 Pa), the tubes were clamped to maintain the vacuum.

8. 300 mL of SC-15 were prepared with a 1:0.3 ratio of resin and hardener. Air bubbles were removed from the resin mixture using a vacuum chamber.

9. The resin was infused into the vacuumed assembly through an opened air channel using a funnel. Resin needs to flow continuously; otherwise voids will form inside the joint. Once resin was seen to flow through the assembly and out the other end, both tubes were again clamped to assure that saturation of the preform was maintained. The assembly then was left at ambient room temperature to cure for 24 hours.

10. Next, the assembly was cured inside an oven at 94°C for 4 hours.

11. After the resin inside the joint complete cured, the mold parts were removed from the assembly to yield a bulk of aluminum pi-joints. **Figure 3-6** shows an end view of the completed joint.
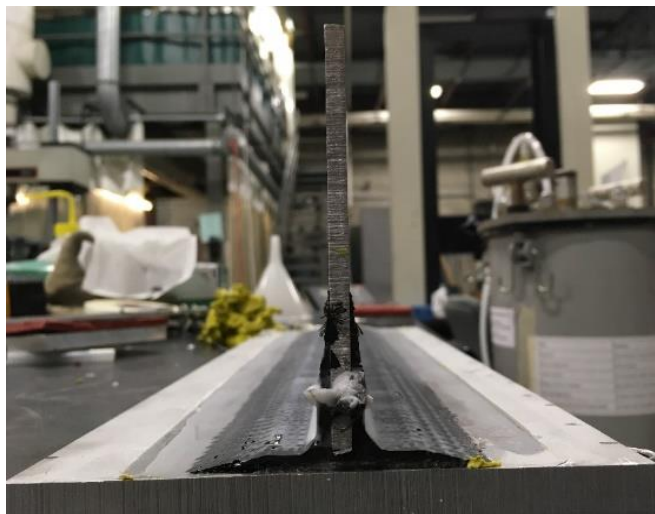
Figure 3-6. The bulk of Aluminum Pi-joints after curing

12. Finally, with a metal band saw and later a diamond abrasive saw, the joint was cut into 2 inch thick individual joint specimens as shown in **Figure 3-7**. The end pieces were discarded. Individual pi-joint specimens ready for testing are presented in **Figure 3-8**. The one end of each specimens then were coated with photoelasticity coating.
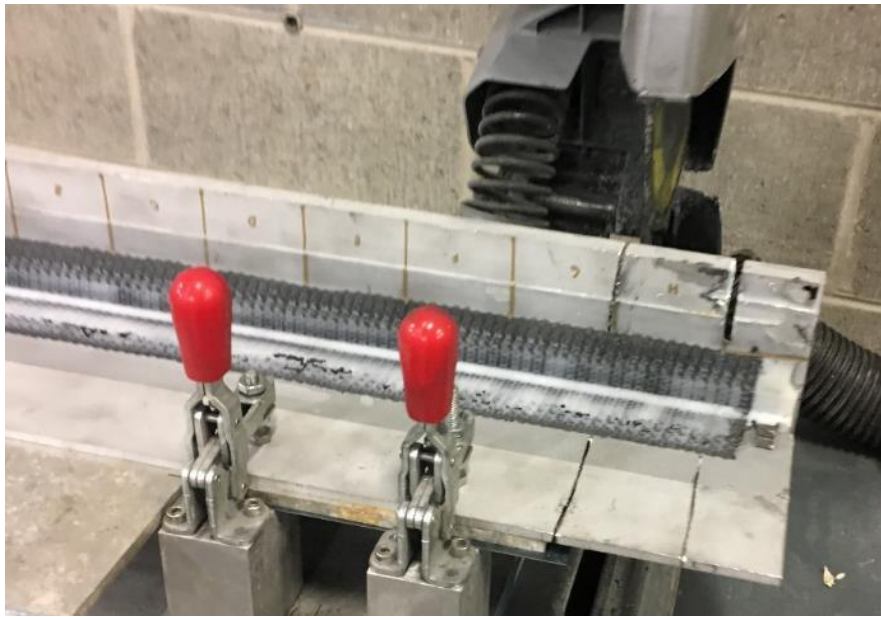
Figure 3-7. Pi-joint cutting with an abrasive diamond saw
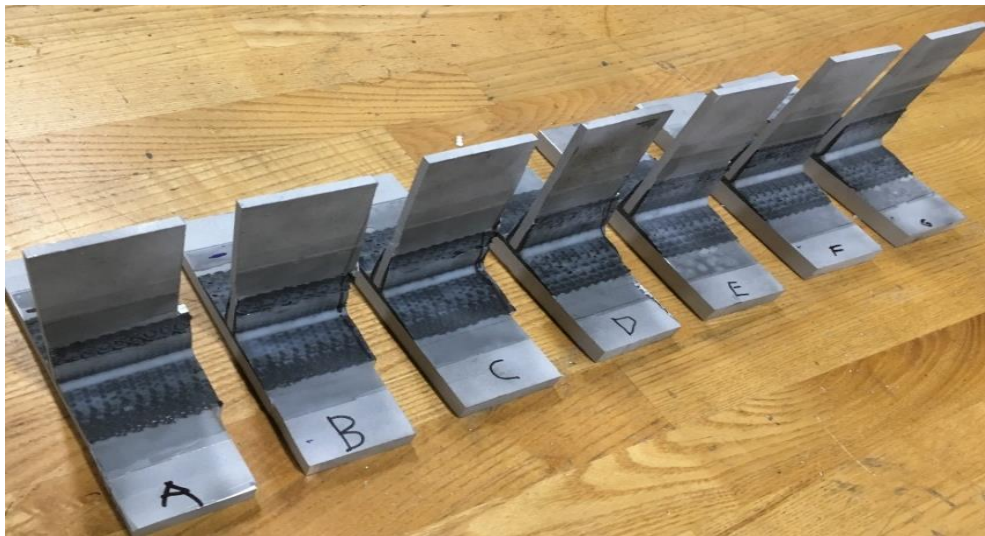
Figure 3-8. Individual aluminum pi-joints after cutting

In the end, batches of 3 types of aluminum pi-joints were tested; one type was pristine, and two types were fabricated with a 10 mm wide delamination that differ in the locations. **Figure 3-9** illustrates the types of joint tested in the experiment. **Figure 3-9 (a)** is a pristine joint sample. **Figure 3-9 (b)** is a pi-joint with a delamination located in the middle of the preform-base interface. **Figure 3-9 (c)** shows the joint that contains the delamination on the side of the preform-base interface.
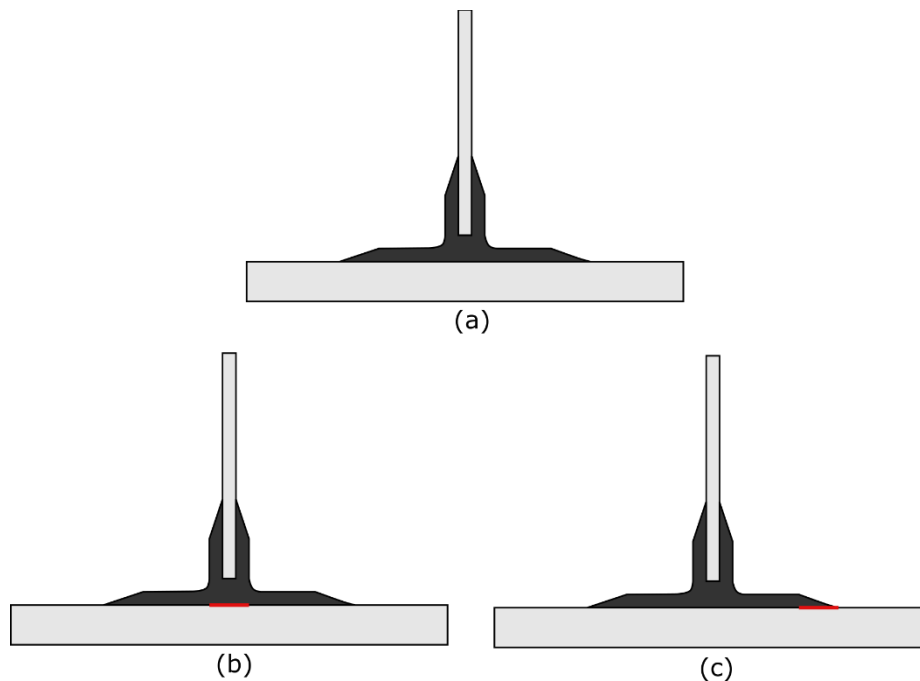
Figure 3-9. Three pi-joint types in this experiment. (a) healthy joint (b) 10 mm delamination in the middle (c) 10 mm delamination on the side.

3.2 Photoelasticity Coating Selection for Aluminum Pi-Joints

Photoelasticity coatings are generally made of transparent birefringent materials which doubly refract light when loaded and illuminated in polarized light. Historically, there have been several types of materials used for photoelasticity coatings, such as polyurethane [27], gelatin [19], polycarbonate, and epoxy resin. Currently, photoelasticity coatings are commercialized by Micro-

measurements ® and mostly made with epoxy resins. In conjunction, they also produce specialized adhesives to bond the coating.

The selection of photoelasticity coating type is analogous with the importance of choosing a gage and glue for resistance strain gage experiments. Specifically, for coating application on aluminum pi-joints, there are several factors that are important, namely: coating forms, sensitivity, reinforcing effect, and environment temperature effects.

1. Coating Forms

Photoelasticity coatings are available in two forms: solid flat sheets and liquid for contour surface applications. In this research, the flat end surface of the pi-joints is of main interest for strain measurement. Hence, a solid flat sheet type coating was suitable. Before the coating is applied, it is also important to apply a reflective/scattering backing in the surface-coating interface area so that adequate light will be reflected back to the analyzer and sensor.

2. Sensitivity

Coating sensitivity is defined as the principal strain difference needed to generate a single isochromatic fringe. Mathematically it is defined as:

$$f = \frac{\lambda}{2tK} \tag{3.1}$$

With f is the strain sensitivity coefficient (μm/m or μin/in), λ is the wavelength from the light source, t is the coating thickness, and K is the strain-optic coefficient. From formula (3.1), it can be concluded that for a high level of strain measurement, i.e., in the plastic region, a higher value of f (less sensitive coating) us required. On the other hand, for low strain level measurement, a more sensitive coating is required (lower f).

In order to achieve high sensitivity, a stiffer material type must be chosen to increase the strain-optic coefficient (K). The other way is to increase the thickness of the coating. However, increasing

38

sensitivity might come at the cost of reinforcing effects from the coating. Thus, a careful coating selection and compromise is required to measure strain for the case in hand. A convenient coating material selection chart from Micro-measurements ® is presented in **Table 3-1**.

Table 3-1. Micro-measurements ® coating material options, adapted from [28]

Coating Material	Maximum Elongation	Typical Application
PS-1	5%	Testing on metals, concrete, glass, and hard plastics in the elastic and elastoplastic range
PS-10	3%	
PL-1	3%	
PL-10	3%	
PS-3	30%	Testing on soft materials such as rubber, plastics, and wood
PL-2	50%	
PL-3	>50%	
PS-4	>40%	
PS-6	>100%	Testing on soft materials such as rubber, plastics, and wood

3. Reinforcing effect

Once the coating is glued to the specimen, it will increase the strength of the structural member to some extent. Zandman, Redner, and others have extensively studied the reinforcing effect of birefringent coating in several studies, e.g. [18] [17] [29]. There are four ways in which the reinforcing effect contributes to loss of accuracy in strain measurement [7], namely:

a) The increase of stiffness in the structure due to additional coating

b) Disturbance in the stress distribution because of coating

c) Photoelastic strain reading is averaged through coating thickness

39

d) Traction in surface structure due to mismatch of Poisson's ratio.

Because the coating thickness to specimen thickness ratio is going to be considerably small at 0.02 and because the stiffness of the coating material is much less than that of the aluminum and composite preform, all of the points (a) through (d) that might cause the loss of accuracy in the photoelasticity coating method can be discounted.

   4.   Temperature environment.

Photoelastic testing depends on the temperature on which experiments are performed. If the environment is not at room temperature, a careful selection of coating must be performed to ensure the accuracy of measurement. This is because the strain-optic coefficient of the coating (K) changes its behavior at high temperature. **Figure 3-10** from a Micro-measurements ® technical note [28] illustrates how the coating behaves on elevated temperature. Since this experiment was conducted at ambient room temperature ($< 100^\circ$ F) there will be little to no error due to temperature effects.
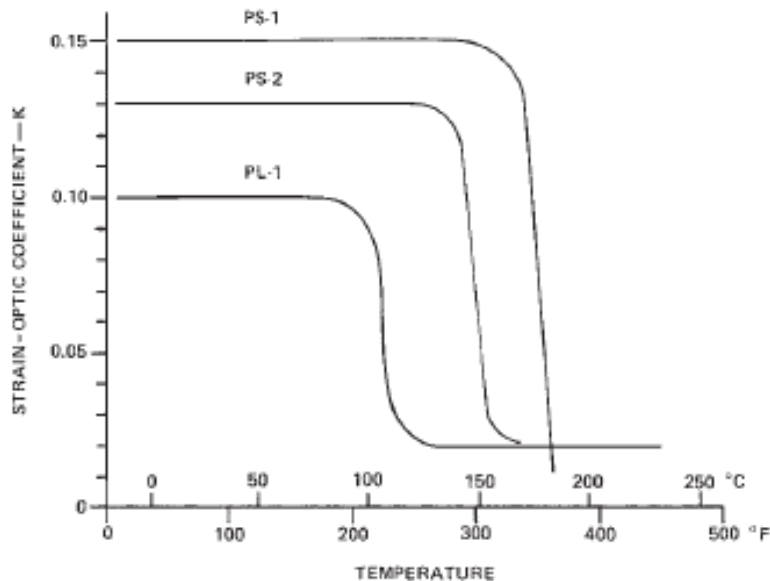
Figure 3-10. Temperature effect on strain-optics coefficient (K) of photoelasticity coating materials [28]

In conclusion, based on the mechanical, optical, and temperature properties of available photoelasticity coatings from Micro-measurements, PS-1A sheet coating with 3 mm thickness was selected for the experiments. Material properties for the PS-1A coating are provided in **Table 3-2**. In order to bond the photoelastic coating, PC-10 adhesive was used. It is a room temperature curing adhesive with curing time of 4 hours and modulus after curing of 3.1 GPa.

Table 3-2. PS-1A Coating Material Properties

Dimension	10x10x0.12 inch
Elastic Modulus	3.1 GPa
"K" factor	0.15
Thickness	0.127 inch
"f" value	597 $\mu\varepsilon$
Backing	Diffuse reflective backing

3.3 Applying Photoelasticity Coating to Aluminum Pi-Joints

To bond photoelastic sheet coating such as PS-1 A to a flat surface (pi-joint surface) is a simple but delicate task. Generally, the sheet must be shaped precisely to match the surface edges and later bonded with the required adhesive. Specifically, instructions on photoelastic coating application are presented through a flowchart in **Figure 3-11** which was derived from Micro-measurements® technical document [30]. **Figure 3-12**. Illustrates the process of applying the photoelasticity coating
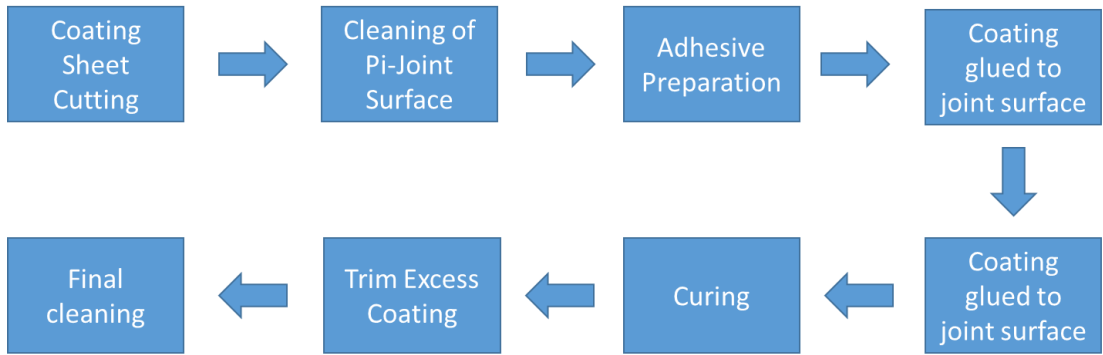
Figure 3-11. Flowchart of applying photoelasticity coating
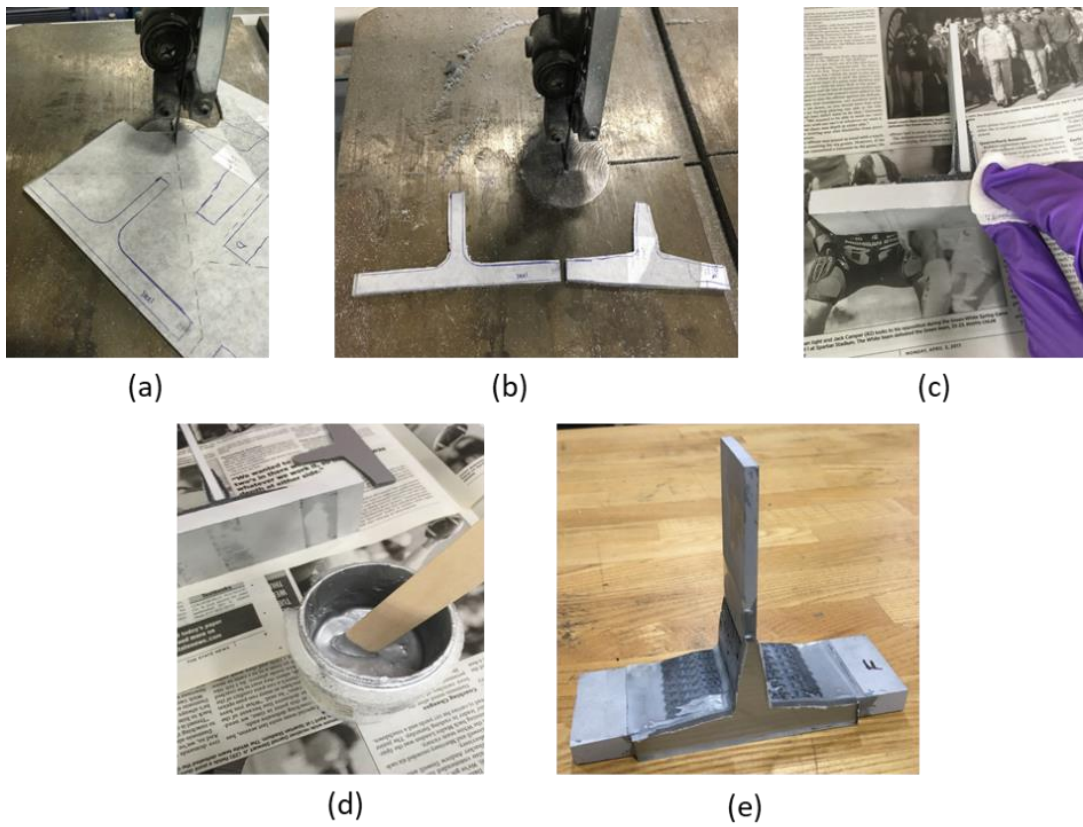
Figure 3-12. Applying photoelasticity coating process (a) cutting coating sheet using band saw (b) coating that has been shaped to the surface of the joint (c) pi-joint surface cleaning (d) PC-10 adhesive preparation (e) pi-joint with bonded coating after 4 hours of curing

Chapter 4 Experimental Testing

4.1 Test Setup

Experimental test on pi-joint specimens were performed at ambient room temperature using an MTS-810 universal testing machine. Specimens were mounted with a specialized grip that allows for a web pull-out with a simple support on the base of the joints. **Figure 4-1** and **Figure 4-2** illustrate the specimen pull-out test. If a gap existed between the support and the base, shims were installed to ensure symmetric boundary conditions. In addition, load-displacement data were recorded using an MTS 634.31 F laser extensometer.

The out-of-plane behavior of the pi-joints was characterized by observing isochromatic fringe patterns that appear during the pull-out test. The experimental setup to record the fringes consisted of a Nikon D7100 camera with a Nikon 55-200 mm lens, a white light source, and a Micro-measurements ® model 031 reflection polariscope. Isochromatic fringe images were captured with camera settings of low aperture (f-5.6), high shutter speed (1/40 s) and high ISO (640). This setting was used to ensure the clarity of the fringe pattern from the coating. All of the equipment was assembled and located 1 m from the specimen. The equipment is shown in **Figure 4-3.**
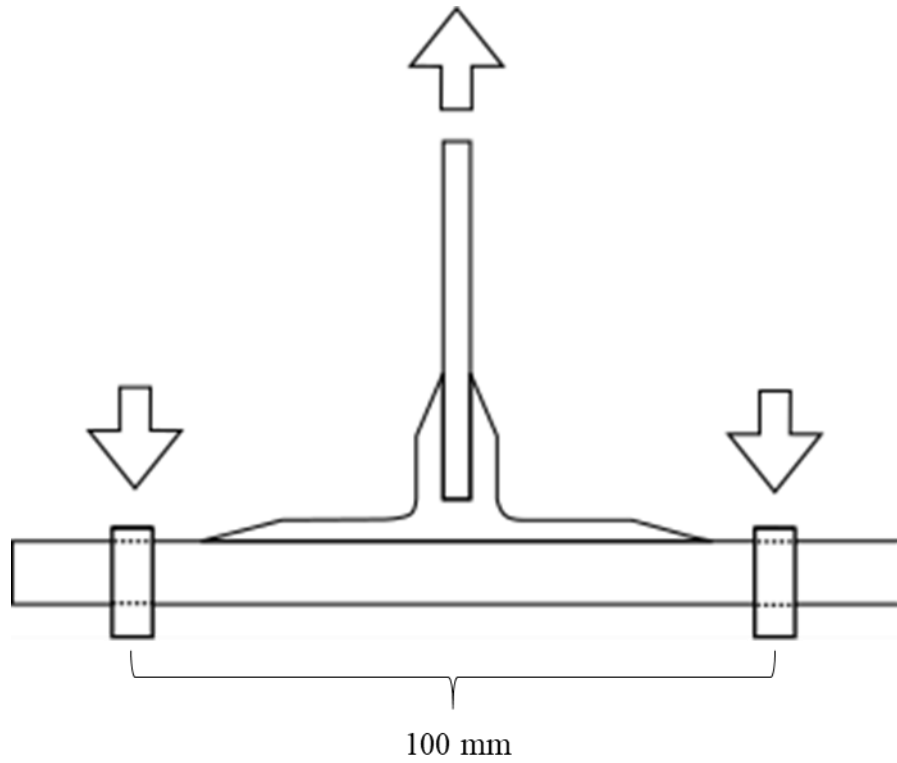
Figure 4-1. Schematics of aluminum pi-joint web pull out with symmetric constraints in the span of 100 mm
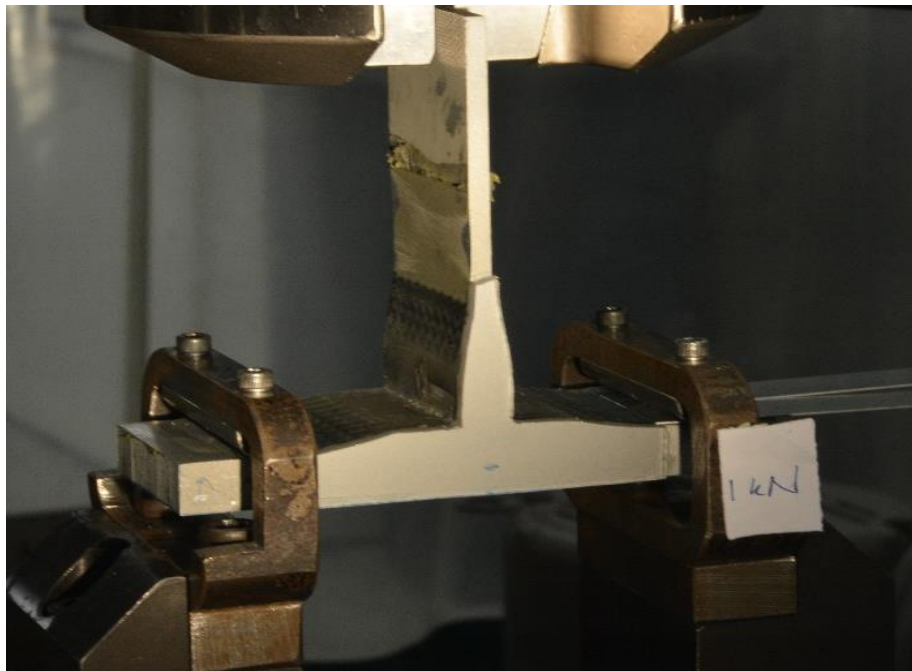
Figure 4-2. Coated Pi-joint during the pull-out test

Mounted specimen on MTS-810 Machine

Reflection polariscope

Digital Camera

Light source

Figure 4-3. Experimental Test Setup

4.2 Test Procedure

Before testing the aluminum pi-joint specimens, a T-steel specimen with a birefringent coating was tested in order to check the functioning of the reflection polariscope, to refine test procedures, to establish symmetric loading, and to ensure coating suitability. The T-steel specimens was made from a rolled steel I-beam stock cut into a 24 mm thick specimen. The T-steel specimen is shown in **Figure 4-4**. The PS-1A coating used for pi-joints specimens were applied to the steel as well. The T-joint coated was loaded in the MTS-machine until the first three isochromatic fringe orders could be seen. Then, the fringe patterns caused by the load were compared with a numerical simulation for the T-steel specimens.

Figure 4-4. Steel T-joint specimen with 24 mm thickness.

The aluminum pi-joints were divided into two groups that were to be subjected to differing test protocols having different objectives. The first group of tests were conducted to obtain the mechanical properties, namely the pull-out load-displacement profiles as well as the failure loads and modes. These tests were erformed on samples that did not carry any photoelastic coating. The second group of experiments used photoelasticity to characterize the strain distributions within the pi-joints.

The pull-out test was conducted with the rate of crosshead displacement 1 mm/min until joint failure. The load-displacement profiles for these failed joints were recorded and the failure modes were analyzed.

The joints having the photoelastic coating were loaded incrementally in 0.5 kN steps from 0 load until three isochromatic fringe orders were observed in the regions of highest stress. These pi-joints were not loaded until failure in order to preserve the specimens and also to maintain elasticity

requirements for photoelasticity analysis. For each load increment, isochromatic fringe patterns were captured in both dark-field and light-field polarization to capture whole- and half-order fringes that appear during the test, thus enhancing sensitivity. In total, six aluminum pi-joint specimens were tested in this experiment, consisting of three pairs of both uncoated and coated pi joints. **Table 4-1** describes the type of joints tested and the corresponding specimen labels.

Table 4-1. Six Aluminum Pi-joint types and labels

Type		Label
Healthy	Uncoated	A-1
	Coated	A-2
Middle-delamination	Uncoated	B-1
	Coated	B-2
Side-delamination	Uncoated	C-1
	Coated	C-2

Chapter 5 Numerical Simulation

A numerical simulation was devised to aid in interpretation of the experimental data from the photoelasticity coating studies and the mechanical testing. Results from numerical simulations can improve insight into the complex pi-joint failure mechanisms and might be used in future work as an experimentally validated model for design purposes. In this study, simulations of aluminum pi-joint behavior were designed using the widely used finite element program ABAQUS ®.

First, numerical simulation was performed on the T-steel specimen to compare strain distributions obtained from the preliminary pull-out test. T-steel was designed as a two-dimensional plane stress model with 0.5 mm-sized quadrilateral nodal elements and constrained on both flanges with the span of 100 mm; as shown in **Figure 5-1**. Properties to model the T-steel deformation were taken from the Steel A-992 properties list and are presented in **Table 5-1**.

Table 5-1. T-Steel properties used in the numerical simulation

Steel A992 Properties	
Modulus (GPa)	204
Poisson's Ratio	0.29
Yield Strength (MPa)	374
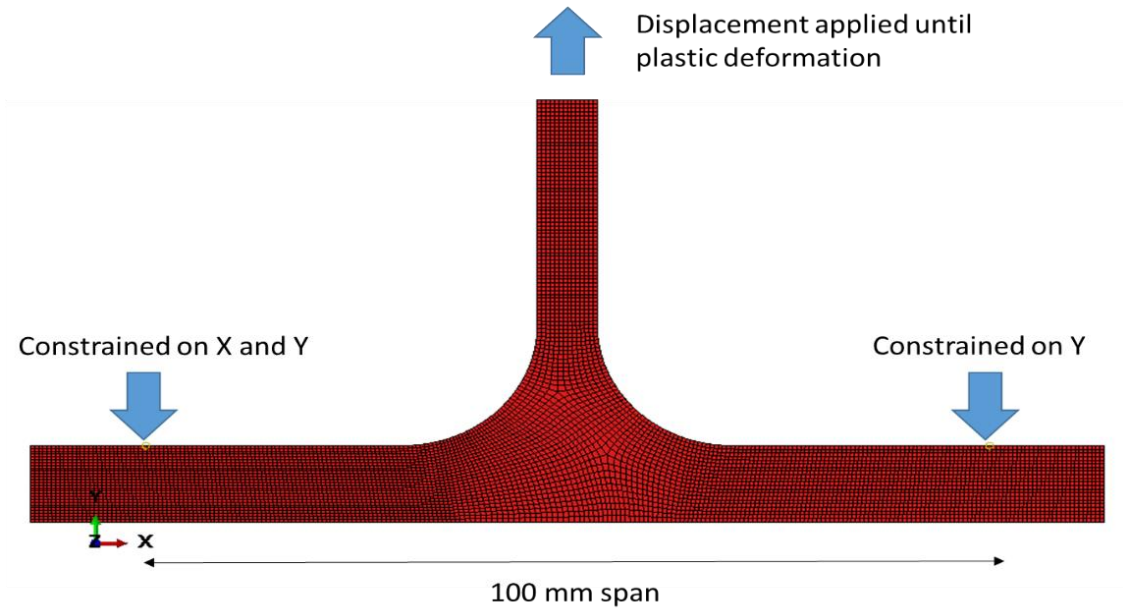
Figure 5-1. T-steel numerical simulation in ABAQUS ®

Numerical simulations for aluminum pi-joints were then constructed for comparison with the results of the photoelaticity studies. Two-dimensional plane stress model of the aluminum substrates, carbon fiber preform, and adhesive were built separately and subsequently assembled using surface interactions with tie constraints. 0.5 mm quadrilateral nodal elements were used for the substrate and the preform. In contrast, the adhesives were modeled using a smaller mesh size that is equal to the bond-line thickness (0.127 mm), meaning that the bond line consisted of only one layer of elements. Details of the loading condition for the pi-joints and the element meshes are shown in **Figure 5-2.** A total of 11272 elements and over 12000 nodes were used in these computation, which were run on a Michigan State University Department of Engineering Computer Services (MSU DECS) remote access server computer.
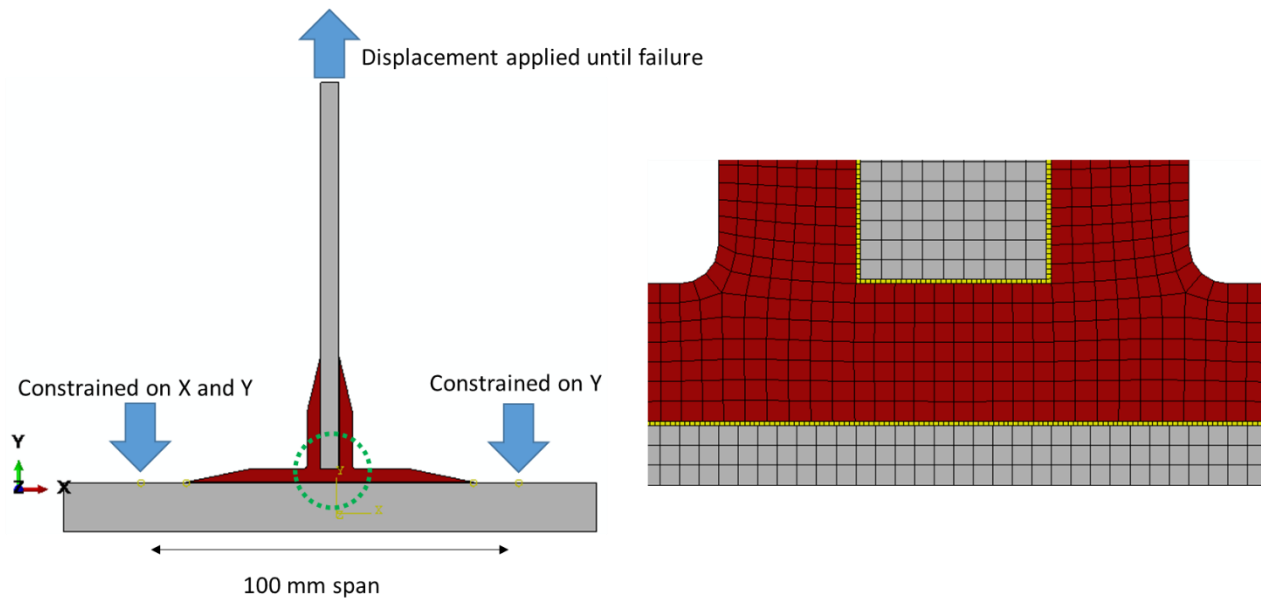
Figure 5-2. Pi-joint numerical simulation and mesh condition in ABAQUS ®

The SC-15 resin was modeled in detail using cohesive elements, and the delamination behavior was modeled with a traction-separation response. Bonding forces are present with the traction stress during considerably small displacements. Once the damage criteria are reached, separation occurs while displacement continued until complete separation. The damage evolution or de-bonding was modeled in detail by defining the fracture energy as a function of the mixed modes using the analytical power law fracture criterion. The fundamental theory of cohesive modeling is thoroughly discussed in [31] [32].

Material properties for modeling of aluminum pi-joints were taken from various pieces of literature and are in general similar to the numerical simulation of pi-joints published by Sebastian [4]. These properties for pi-joint modeling are given in **Table 5-2**. The adhesive was modeled to have a thickness aspect ratio of unity (1) prior to load application, then it thins out and breaks after loading. In the end, load-displacement and strain distribution patterns were obtained for each case of the tested pi-joints.

Table 5-2. Aluminum pi-joint properties used in the numerical simulation

Adhesive SC-15 Properties [33]	
Modulus (GPa)	2.685
Tensile Strength (MPa)	58.1
GIc (J/m^2)	132
GIIc (J/m^2)	460
Aluminum	
Modulus (GPa)	68.9
Poisson's Ratio	0.33
CFRP Preform [34]	
Isotropic Modulus (GPa)	32.8
Poisson's Ratio	0.3

Chapter 6 Results and Discussion

6.1 T-Steel Specimen

The T-Steel specimen with 24 mm thickness was experimentally tested in a pull-out configuration in the elastic range of the metal. Load-displacement data from both experiment and simulation were obtained and are presented in **Figure 6-1.** The slope from both curves indicates good agreement between simulation and experiment. The testing of the specimen was not carried into the plastic range of deformation so that the specimen can be re-examined in the future, if needed.
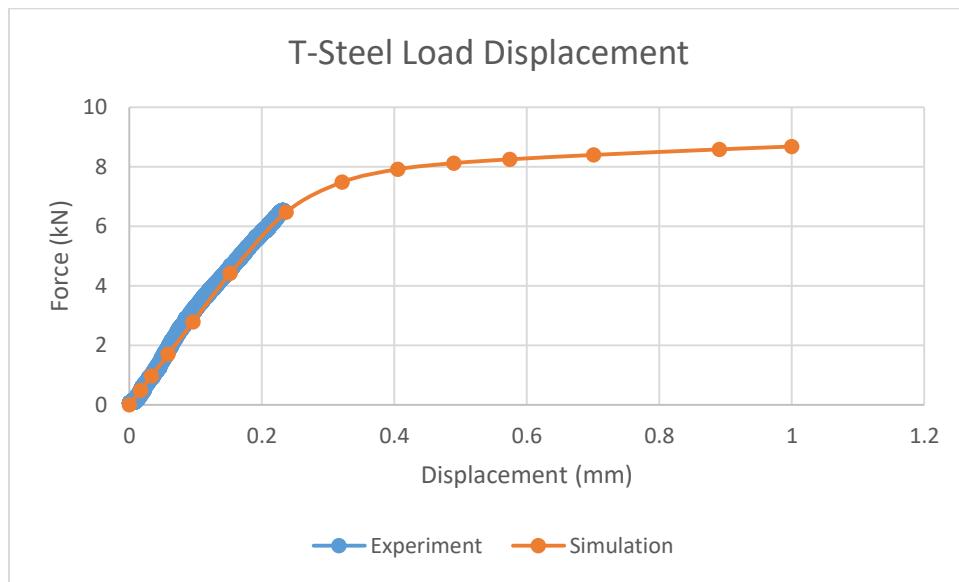
Figure 6-1. Load-Displacement curve of T-Steel Specimen

Initially, isochromatic fringes on the steel specimen were captured before any load was applied. This image serves as a baseline for analysis of images captured under load. The coating was also marked during initial setup to show the center location of the joint. The marker location would be near the neutral axis of structural bending during the pull-out test, as is observed in traditional 3-point bending of a beam. **Figure 6-2** presents the isochromatic fringe image of the T-steel specimen at zero load. The dark color on almost all of the joint surface indicates that little or no strain is present.
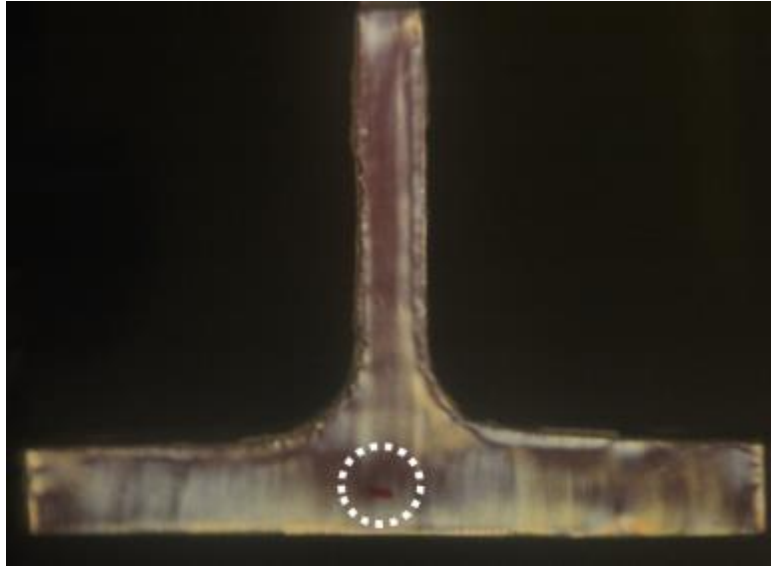
Figure 6-2. T-Steel specimen isochromatic fringe order during zero load and dark field polarization. The white circle indicates the location of the neutral axis marker.

Next, the load was increased incrementally until the first fringe order was clearly observed. The numbering of the fringe orders was based on the color criteria from the manufacturer as shown in **Figure 6-3** for "white" light. It is important to note that sensitivity of the photoelasticity coating method is greatly limited when relative retardations are obtained from simple judgements of color. The results observed depend on the color spectrum of the light source, the response of the photographic system, and, critically, the eye of the observer. Calibration with the light source and other apparatus used is necessary for the best accuracy of results, but these steps were not implemented. Further, refined techniques for measuring the relative retardation are in common use, but were not incorporated into these preliminary studies.

Generally, fringe orders start to emerge in the regions with highest shear strain and migrate to regions of low strain. The first fringe order was visible at a load level of 1.5 kN, as shown in **Figure 6-4**, which includes the light field results showing half-order fringes. Following recording of the first fringe order, the load was increased until the second fringe order came into view. **Figure**

53

6-5 presents the isochromatic fringe pattern at 4 kN load, where in the maximum fringe order is slightly more than 2.

Figures 6-4 and **6-5** indicates that the location of the neutral axis of the steel flange aligned reasonably well with the zero fringe order on the isochromatic patterns. The markers were in line with the dark fringe from dark-field polarization and with the light fringe obtained with the light-field polarization. The high strain area was observed, as expected, to be in the lower part and the upper part of the steel flange, forming curved lines with similar color. Symmetry of loading is reasonably good but could be better, as indicated by the isochromatic fringe patterns.

Color	Fringe Order N
Black	0.0
Pale Yellow	0.60
Dull Red	0.90
Red/Blue Transition	1.00
Blue-Green	1.22
Yellow	1.39
Rose Red	1.82
Red/Green Transition	2.00
Green	2.35
Yellow	2.50
Red	2.65
Red/Green Transition	3.00
Green	3.10

Figure 6-3. Color fringe numbering criteria from Micro-measurements ® [35]
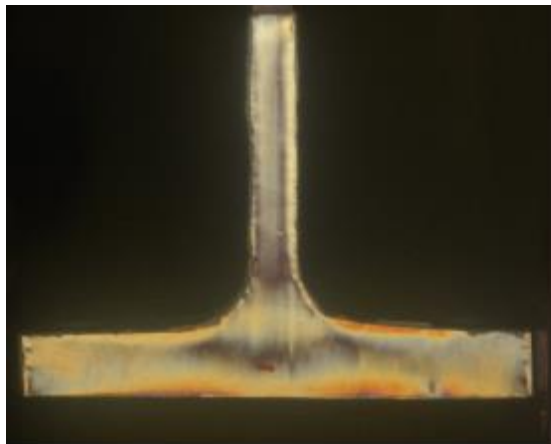
Dark Field Polarization – 1.5 kN load
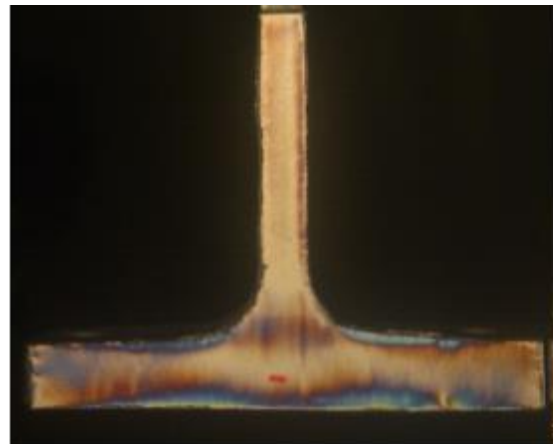
Light Field Polarization – 1.5 kN load

Figure 6-4. Isochromatic images of T-steel specimen at 1.5 kN load.
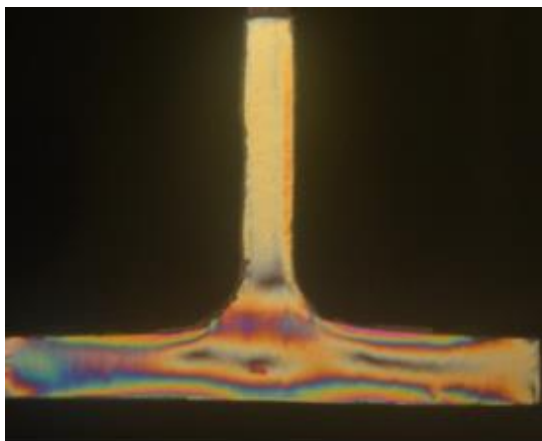
Dark Field Polarization – 4 kN load
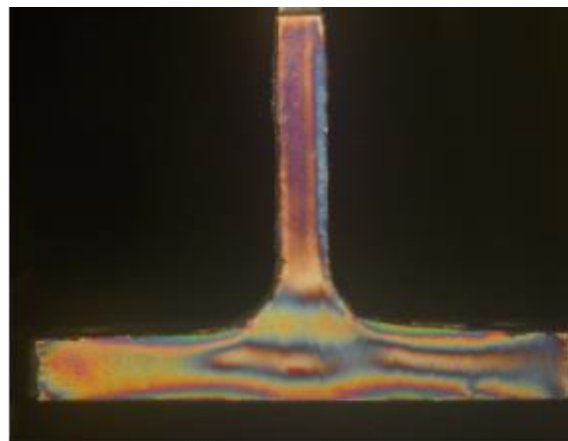
Light Field Polarization – 4 kN load

Figure 6-5. Isochromatic images of T-steel specimen at 4 kN load.

The result from the numerical simulation for a load value of 3.4 kN is presented in **Figure 6-6.** Symmetry of strain distribution was imposed in the simulation. All strain values can be determined for all region of the simulated joint. Extrapolation was performed on the numerical simulation data to yield an estimate of the principal strain values at 4 kN load. Hence, the strain values from the numerical simulation can be quantitatively compared with the experimental data from the photoelasticity measurement.
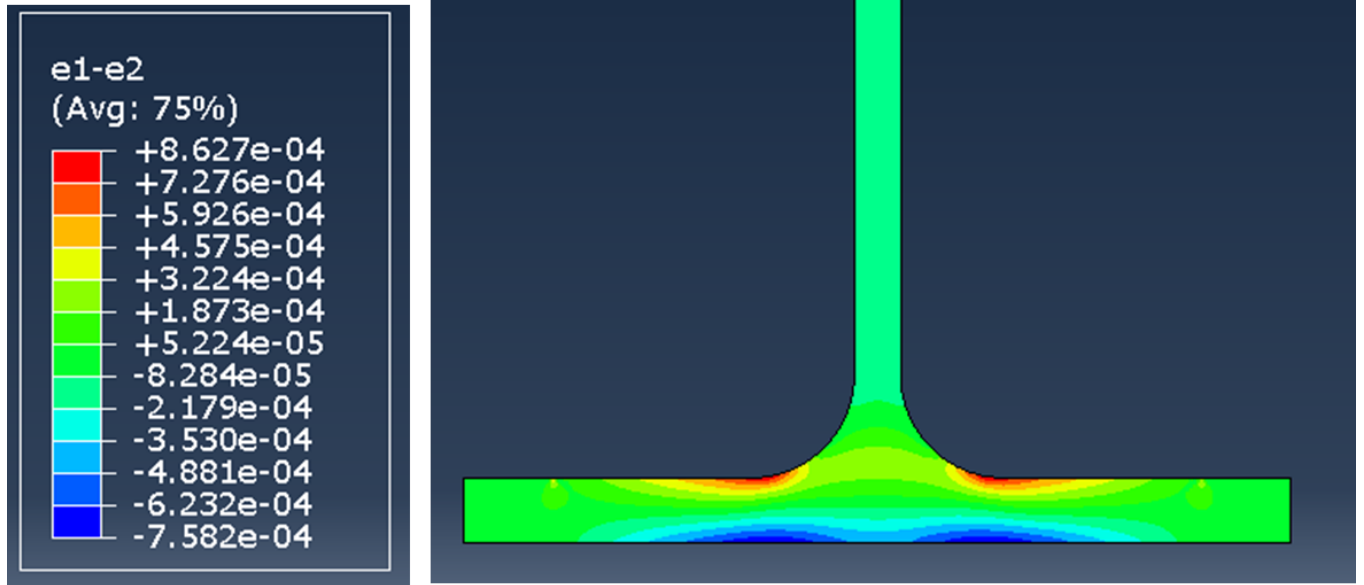
Figure 6-6. Simulation result (principal strain difference maps) for T-steel pull-out load at 3.4 kN load.

An in-depth comparison of the strain distributions between the photoelasticity results and the numerical simulation of the steel joint is presented in **Figure 6-7**. First, numbering of the fringe order was performed on the dark-field polarization image for the 4 kN load level. The numbering guidelines from **Figure 6-3** indicates that the second fringe order corresponds to areas showing the transition from faint red to faint green color. The faint green shows slightly at the bottom of the flange, indicating that the fringe order there is slightly more than 2, say 2.2. The highest principal strain difference value was calculated from the fringe order. Thus, the highest principal strain value difference for 4 kN loading on the coated T-steel joint was found to be:

$$\Delta\varepsilon_{exp} = (\varepsilon_1 - \varepsilon_2) = 2.2 \cdot 597 = 1313 \, \mu\varepsilon = 1.313 \times 10^{-3} \, mm/mm$$

The numerical simulations and further extrapolation of the linear data, gives the value for the principal strain difference as:

$$\Delta\varepsilon_{sim} = (\varepsilon_1 - \varepsilon_2) = 9.042 \times 10^{-3} \, mm/mm$$

Hence, the difference between the two measurement values can be defined and calculated as:

$$\%difference = \left| \frac{\Delta\varepsilon_{exp} - \Delta\varepsilon_{sim}}{\Delta\varepsilon_{exp}} \right| \times 100\% \qquad (6.1)$$

$$\% \, difference \, (steel \, joint) = 31.13 \, \%$$
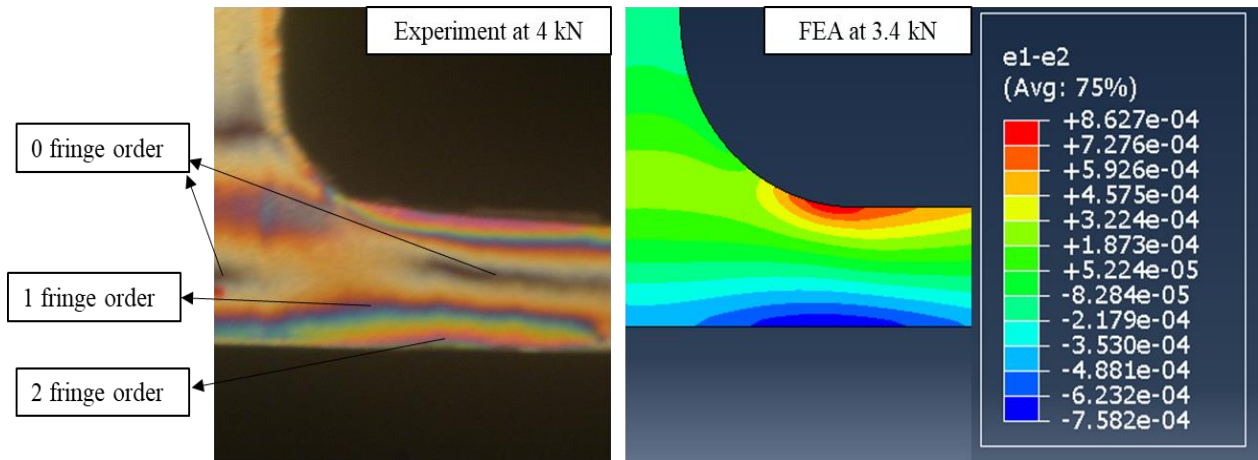
Figure 6-7. Comparison of isochromatic fringe pattern and finite element analysis result of a T-steel joint

Results of the comparison between experimental photoelasticity data and numerical simulation from the preliminary test on the T-steel specimen shows that the agreement is not very good. The discrepancies are probably result from the elementary method of judging fringe order, the unknown color spectrum of the light source, and the limitations of the numerical model. The load-displacement curves were closely matched, but, of course, that does not imply that the strain distributions will match. Qualitatively, the strain maps have similar patterns and clearly indicate corresponding highly stressed regions. As mentioned, the accuracy of experimental data could be increased by improving the technique. All in all, this preliminary test showed the capabilities of both methods to determine strain in a pull-out T-steel joint and provided guidance as to how the methods might be applied to the more complex pi-joints.

6.2 Pristine Pi-Joint

An uncoated pristine or healthy pi-joint, specimen A-1, was tested until failure and the load-displacement data were recorded. **Figure 6-8** presents the comparison of the load-displacement curves found through experiment and simulation. The slopes of the two load-displacement profiles show good agreeability, suggesting that simulation results in the elastic range could be compared with the results from photoelasticity.
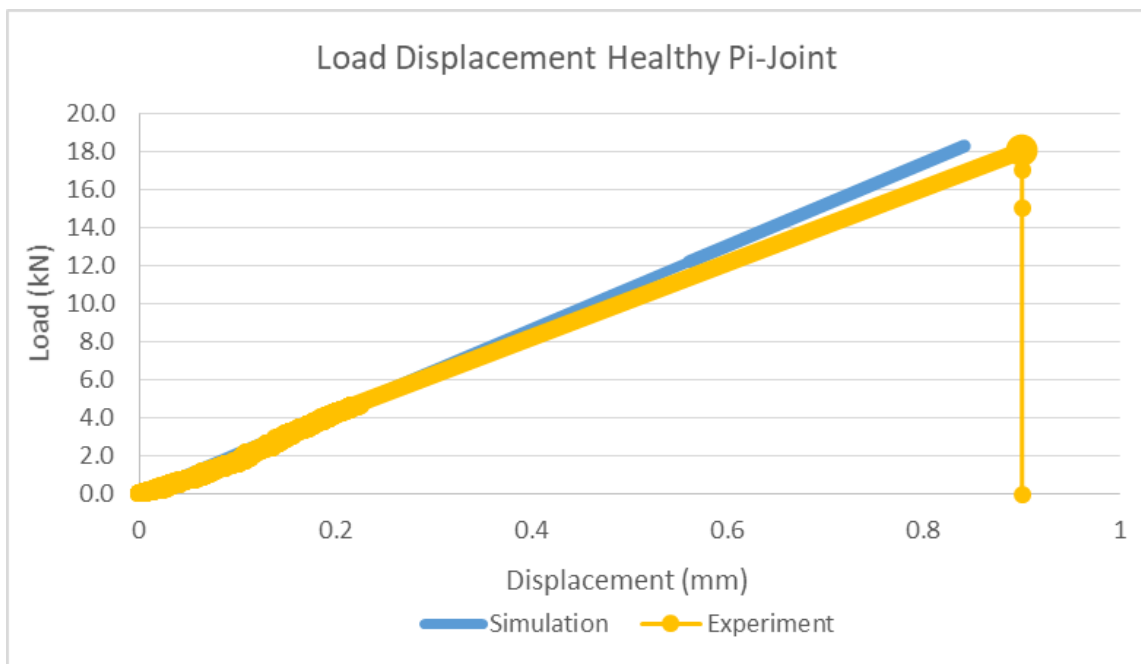
Figure 6-8. Load-displacement data for pristine pi-joint, specimen A-1.

During the constrained web pull-out, the pi-joint specimen did not show any visible signs of deformation. Once the specimen load reaches aproximately 18 kN, however, failure happens instantaneously on the preform-base interface. Audible cracking was heard moments before the critical failure. This failure condition presents a challenge in using these out-of-plane joints in a real structures, where failure is not visible and the load carrying capacity drops significantly and precipitously. **Figure 6-9** shows the pi-joint specimen failure that occurred during the pull-out test.

Both surfaces of the failed specimen A-1 were examined **Figure 6-10** presents the condition of the failed specimen,on the preform's surface and on the base's surface. Cured resin was present on both of the surfaces, which indicates cohesive failure of the resin bond. Hence, the adhesive successfully bonds the aluminum surface to the preform, creating an out-of-plane dissimilar joint. In addition, no failure was observed in the web-preform interfaces. This double-bond area, which acts similar to a double lap shear joint kept its bond integrity and transferred the load directly to the preform-base interface.

Figure 6-9. Complete separation of the base from preform during the pi-joint pull-out test.

Figure 6-10. Specimen A-1 failure condition. Left-preform's surface, Right-base's surface.

The specimen A-2, which had a photoelasticity coating, was tested within the elastic range. The initial isochromatic fringe image was captured and the neutral axis was marked in the center, as presented in **Figure 6-11.** In the dark-field configuration, the coating shows no fringes, indicating that there was no residual stress in the coating and that no strain was present in the structure. The specimen was then loaded and Isochromatic fringes were captured in both dark-field and light-field configurations at various loads. The results for loads of 2 kN and 5 kN are presented in **Figure 6-12** and **Figure 6-13.**
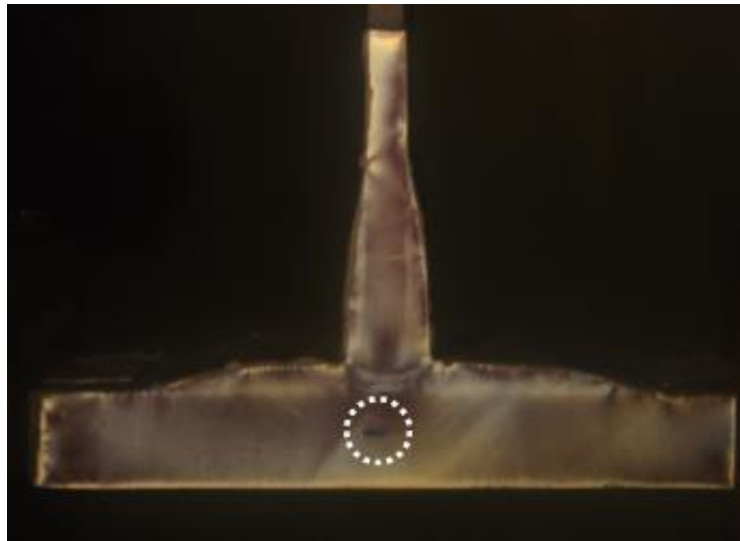
Figure 6-11. Specimen A-2, isochromatic fringe image during zero load**s** and dark-field configuration.

The neutral axis for the base of the joint was aligned with the zero fringe order, as shown in **Figure 6-12**. This figure also shows that the first fringe orders for dark-field polarization emerged on the lower surface of the joint base and quite symmetrically on the composite preform. The isochromatic fringe order from the light-field setup verifies the location of the neutral axis, since the first white fringe represent zero fringe order. **Figure 6-13** presents the isochromatic fringe images at the higher load of 5 kN. Use of the color chart of **Figure 6-3** shows that the fringe order

present at the center of the basal surface, is about 2.5 ±0.1. Close examination of enlarged fringe photographs suggests that the highest fringe order, approaching 3.0, occurs in the corners of the preform, but attention was focused in this study on the strain distribution in the aluminum web and base. The isochromatic patterns were reasonably symmetrical, suggesting that the specimen configuration and test conditions were good or better.

Dark Field Polarization – 2 kN load   Light Field Polarization – 2 kN load
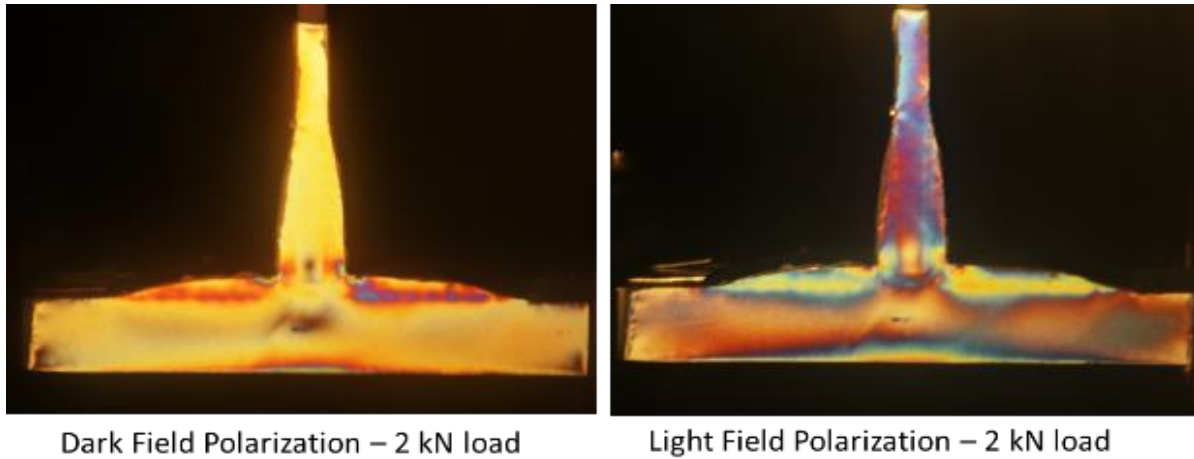
Figure 6-12. Isochromatic images of Specimen A-2 at 2 kN load.

Dark Field Polarization – 5 kN load   Light Field Polarization – 5 kN load
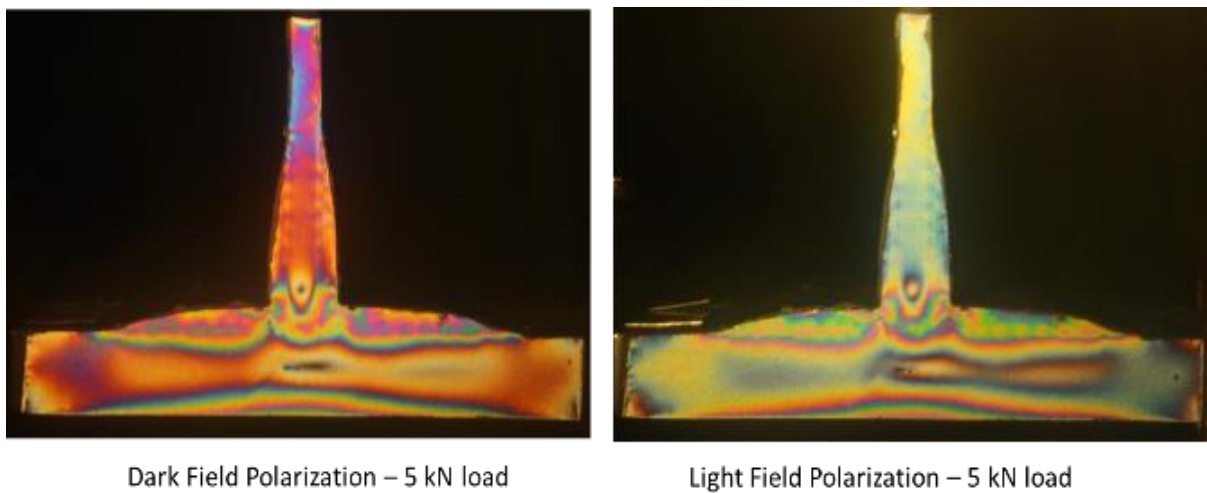
Figure 6-13 Isochromatic images of Specimen A-2 at 5 kN load.

Numerical simulation results for the healthy pi-joint at 6 kN loading are given in **Figure 6-14.** Symmetric strain distribution is forced in the numerical simulation.There is a qualitative similarity between experimental photoelasticity fringes and the simulation's strain maps. The strain values from the simulation were then interpolated to yield strain values for the loading level of 5 kN, so that results from simulation and experiment can be compared.
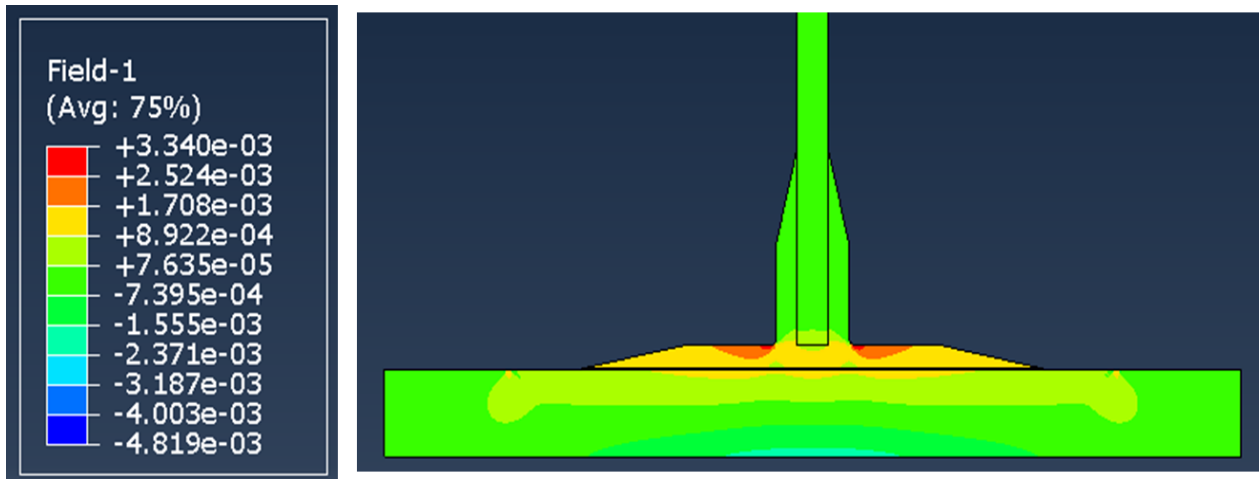
Figure 6-14. Principal strain difference maps from numerical simulation for a healthy pi joint, pull-out load at 6 kN.

The simulation results also give insights into the failure mechanism which occurs in the joint. **Figure 6-15** presents the strain maps during the peak-load. Cohesive elements in the preform-base interface start to fail, then the failure propagates until separation is complete. The location where the adhesive starts to fail in the simulation was close to an area of high strain (red-colored). The same area of high strain was also observed in the photoelasticity measurement results.
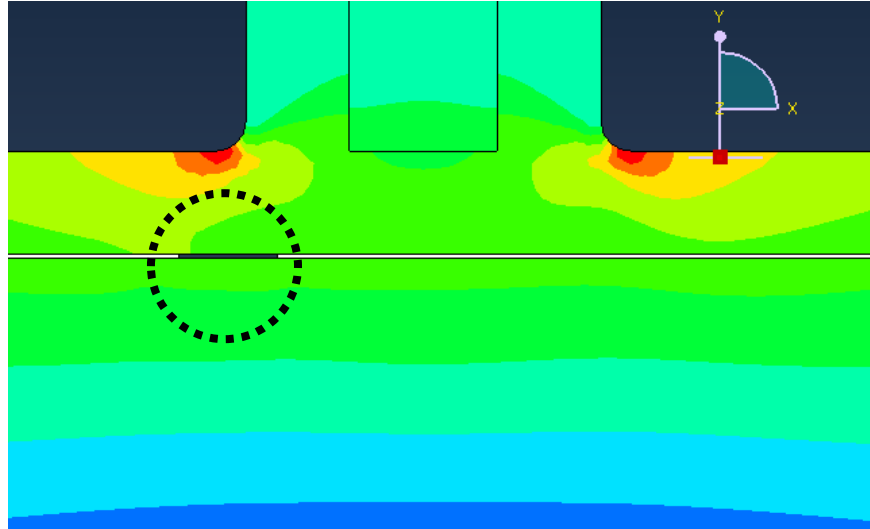
Figure 6-15. Cohesive element failure in the numerical simulation at 18 kN load.

A comparison between the strain maps from experiment and simulation is shown in **Figure 6-16.** The highest fringe order in the isochromatic fringe pattern is above two and located on the bottom of the joint which undergoes bending compressive stress caused by pull-out loading. Another area with high strain values is located on the inside corner of the preform. A quantitative comparison between experimental data and numerical simulation was made by comparing the strain values in the bottom compressive area. Calculations of the principal strain difference from both experiment and simulation, as well as the difference between them, are presented below in **Table 6-1.**

Table 6-1. Specimen A-2 Quantitative Data Comparison.

$\Delta\varepsilon_{exp}$	$2.5 \text{ x } 597 \ \mu\varepsilon = 1.492 \text{ x } 10^{-3} \ mm/mm$
$\Delta\varepsilon_{sim}$	$1.580 \times 10^{-3} \ mm/mm$
%difference	5.86%
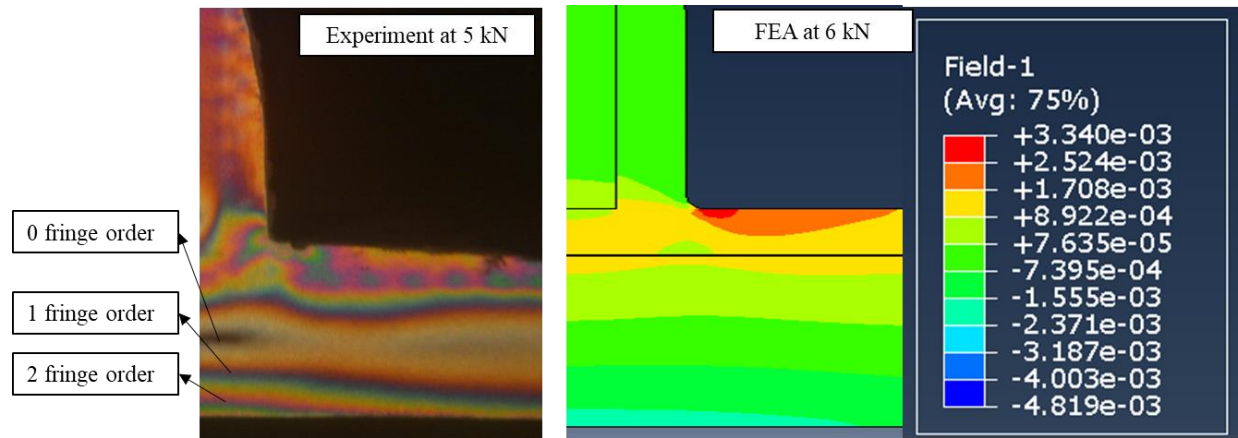
Figure 6-16. Comparison of isochromatic fringe pattern and finite element analysis result on a healthy aluminum pi-joint specimen A-2.

The comparison between the isochromatic fringe images and the numerical strain maps for the healthy aluminum pi-joint shows good agreement in the global qualitative strain distribution and the local quantitative measured strain. Hence, the finite element model is reasonably validated by the experimental photoelasticity coating method. Load-displacement data from the experiment and simulation also were well-matched. In detail, the failure mode of the healthy pi-joint is a cohesive failure which occurred instantaneously. The numerical simulation helps in identifying the initial adhesive crack and the subsequent failure propagation in the joint.

6.3 Pi-joint with middle delamination

Specimen B-1, an aluminum pi-joint with a middle delamination made from Teflon, was tested until failure while load-displacement data were captured. Surprisingly, the joint failed much quicker at the preform-base interface than the healthy pi-joint, and the failure was at a much lower load than that predicted by the simulation, only 2 kN. **Figure 6-17** presents the load-displacement data comparison between the experiment and the simulation. Investigation of the failed joint surface showed no presence of the adhesive on the base, as is shown in **Figure 6-18.** However, joint strength in the web-preform interface was intact. These observations mean that bonding

64

between the composite preform and the metal base was poor. The lack of bonding in the preform-base interface might stem from resin leak during the manufacturing process, from inadequate surface preparation of the metal, or from some form of contamination.
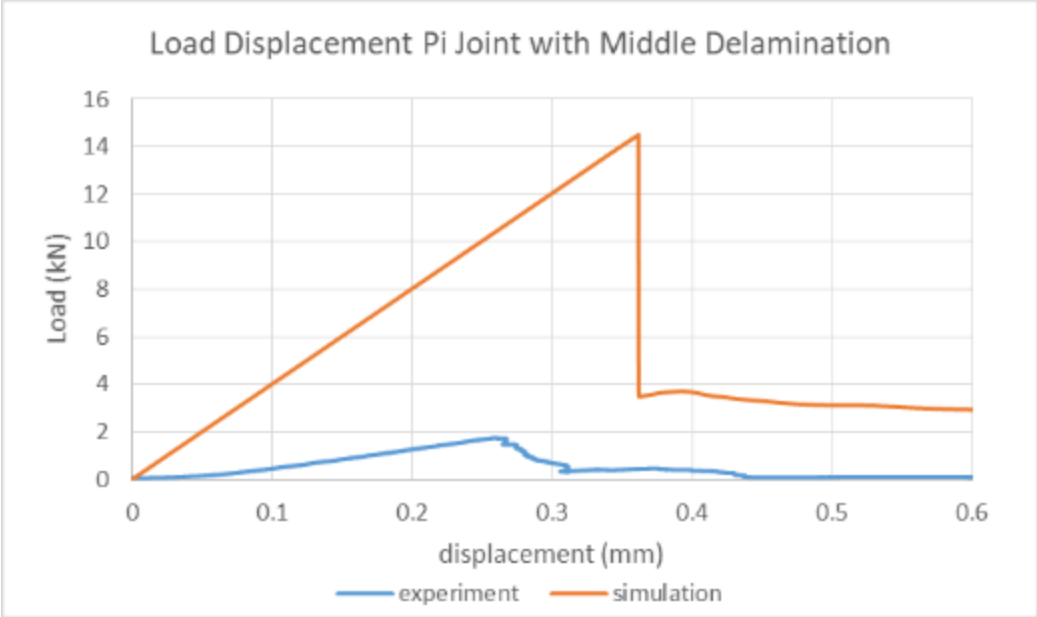
Figure 6-17. Load-displacement data for specimen B-1, pi-joint embedded with middle delamination.

Figure 6-18. Specimen B-1 failure condition. Left-preform's surface, Right-base's surface.

Numerical simulation results show that the pi-joint with the middle delamination was expected to fail around the load of 14 kN. This failure load is 77% of the healthy pi-joint bond strength. However, since the experimental pull-out load was not available, the effect the middle delamination on bond integrity could not be validated. Numerical simulation was also performed to visualize the strain distribution in the specimen. **Figure 6-19** shows that for the delaminated pi-joint at 6 kN load, a symmetric strain pattern was observed. On the middle part of the preform-base interface, strain concentration was present, which indicates the onset of adhesive failure propagation.

The coated specimen B-2 was tested at a very low load level to avoid specimen failure and allow observation of the isochromatic fringe pattern in the linear elastic region. **Figure 6-20** presents the fringe pattern for 0.7 kN loading with both dark-field and light field polarization. Not much information could be inferred from these isochromatic patterns. The pattern poorly resembles the simulation strain map. The delamination appears as colored fringes near the middle part of the joint, but the strain distribution is clearly not symmetrical, indicating possible fabrication flaws or early failure of the adhesive as was found in the pull-out test. Little was learned from this study of a pi-joint with the central delamination except that care must be taken in fabrication of joints that depend on adhesion between dissimilar materials.
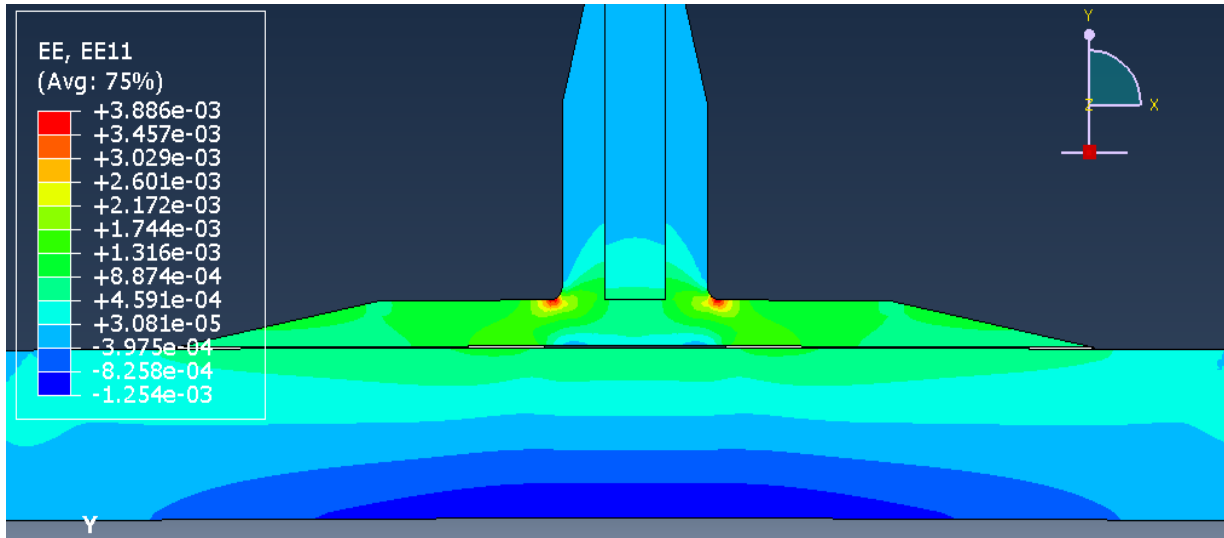
Figure 6-19. Numerical simulation of pi-joint with middle delamination at 6 kN load.

Dark Field Polarization – 0.7 kN load   Light Field Polarization – 0.7 kN load
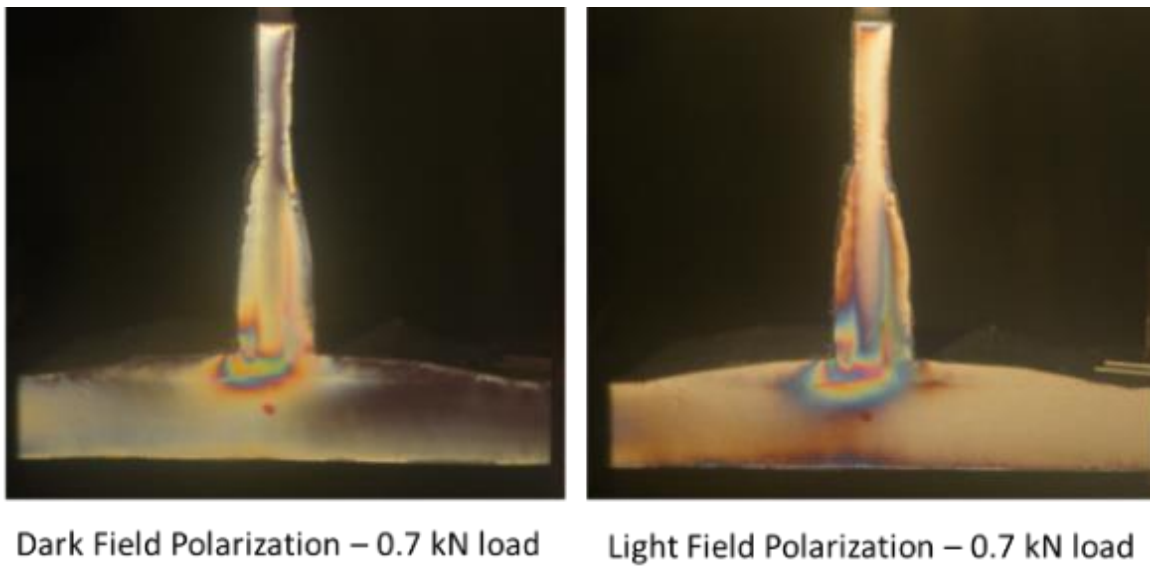
Figure 6-20. Isochromatic images of Specimen B-2 at 0.7 kN load.

6.4 Pi-joint with side delamination

Specimen C-1 was tested until failure in web pull-out configuration while the load-displacement data were captured. **Figure 6-21** shows that the joint failed experimentally at a load of 11 kN which is around 61 % strength of the strength of a healthy joint. A side-delamination reduces strength more than a central delamination with the result that failure occusr more quickly with a lower load.

This is caused by the loss of symmetric load transfer on the pi-joint, and the failure of the can propagate quickly in a manner similar to that of a Mode-1 test sample. **Figure 6-21** also shows that the simulation load-displacement curve agrees pretty well with experimental data. Thus, finite element analysis results can be compared with the isochromatic fringe patterns.

The failure mechanism of specimen C-1 was analyzed by examining both surfaces of the substrate and the preform. **Figure 6-22** shows the surface condition of the metal base and the composite preform. There was cured resin present in both surfaces, which indicates that cohesive failure governs the failure mechanism in the joint web pull-out test. However, it was also observed that some parts of the resin did not completely adhere to the base, especially in the middle part of the preform. This observation indicates that the quality of the joint might be somewhat compromised even before loading, as was the case with the specimen B-1 with the middle delamination.
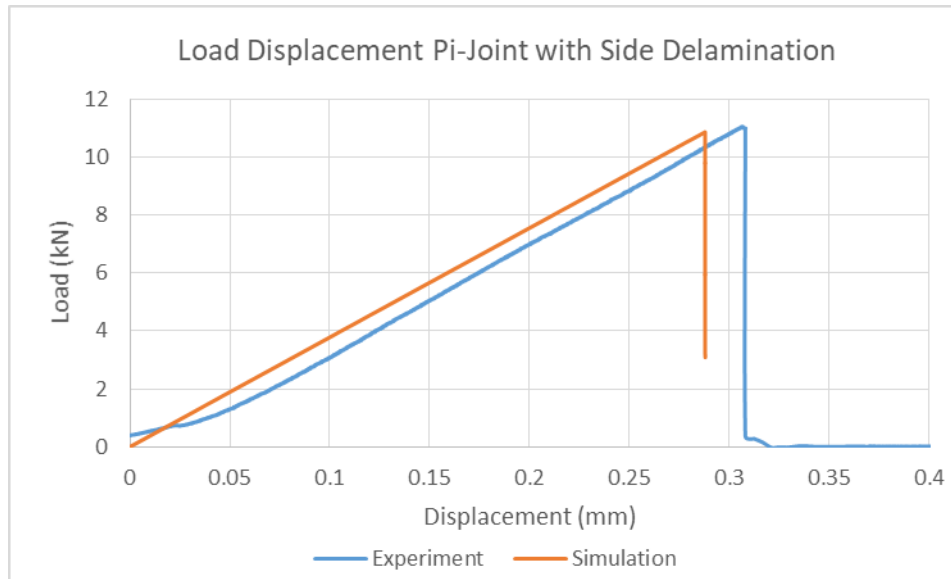
Figure 6-21. Load-displacement data for specimen C-1, pi-joint embedded with middle delamination.

Figure 6-22. Specimen C-1 failure condition. Left-preform's surface, Right-base's surface.

As before, the isochromatic fringe patterns were recorded during pull-out of photoelasticity specimen C-2. The neutral position of the joint was also marked on the surface of the coating. **Figure 6-23** presents isochromatic fringe images of the specimen during loading of 1 kN. The dark-field polarization fringe image indicates the position of the embedded delamination; it is coincident with the narrow emerging red-blue fringe on the left side of the joint just above the 10 mm scale marker that was added to the photograph. The marker confirms the width of the delamination, which is 10 mm. The delaminated area clearly suffers higher strain concentration than the other parts of the pi-joint. Thus, the photoelasticity coating method was able to locate and quantify this pi-joint imperfection.
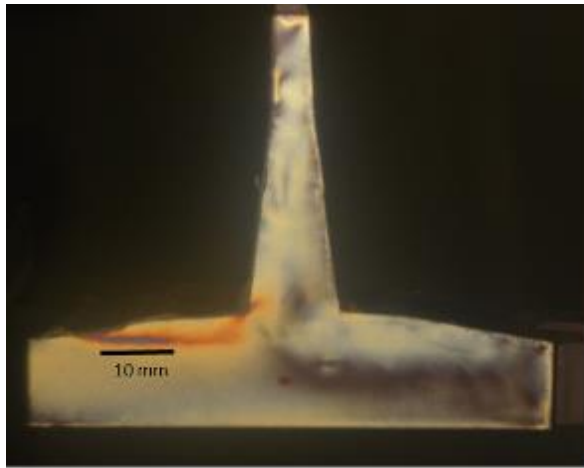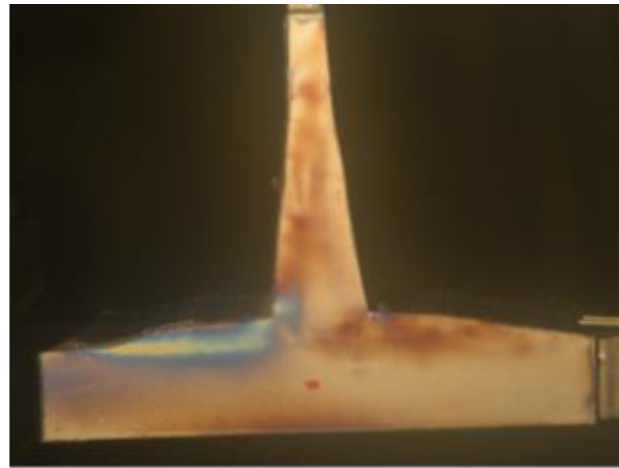
Dark Field Polarization – 1 kN load   Light Field Polarization – 1 kN load

Figure 6-23. Isochromatic images of Specimen C-2 at 1 kN load.

The pull-out load was increased until 2 kN, at which the first fringe order appears, as shown in **Figure 6-24,** on the lower part of the base where compressive stress occurs owing to bending. The neutral axis from the marker aligned well with the zero fringe order on the joint. The isochromatic fringe pattern evolves asymmetrically during the loading, as is to be expected. The fringes in the region of the delamination remain at the same location, however with higher strain level values. Interpretation of the the colored fringes as discussed above indicates that the maximum fringe order at the side-delamination is approximately 2.5, which is more than twice that at the center of the base. The maximum fringe order in the corner of the preform appears to be approximately the same as that found at the delamination.A significant observation is that the fringes surrounding the delamanation remain "closed," which suggests that the outboard end of the crack did not open up. Evidently enough resin found its way to the outside edge of the delamination to maintain structural integrity. In other words, this delamination was not truly of the "edge" type.

70

Dark Field Polarization – 2 kN load   Light Field Polarization – 2 kN load
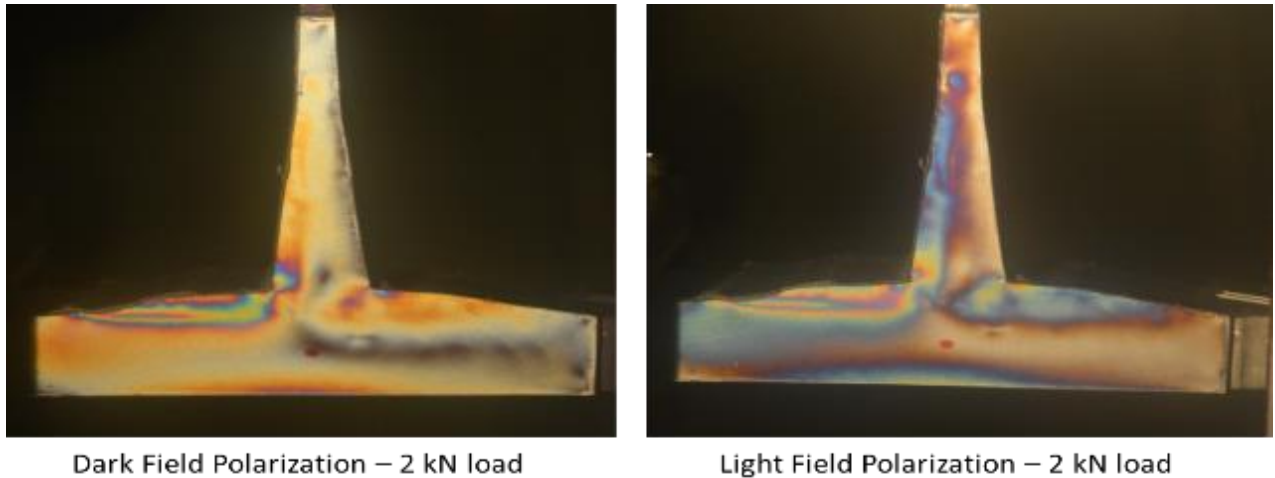
Figure 6-24. Isochromatic images of Specimen C-2 at 2 kN load.

Strain maps from numerical simulation at 1.9 kN load are given in **Figure 6-25.** A comparison of the isochromatic fringe orders and the simulation strain map for the region surrounding the delamination is shown in **Figure 6-26.** The simulation strain maps show a much more symmetric strain distribution in comparison to the experimental photoelastic fringe image. Asymmetry in the numerical simulation occurs on the left side of the joint, which is the delamination side, but it is not nearly as severe as that found from photelasticity nor that expected from knowledge of fracture mechanics and elasticity theory. Poor simulation of the effects of the induced delamination is evident.

Next, quantitative strain values from the isochromatic fringe order data and the interpolated strain value from the simulation were compared Details of the calculation for the quantitative comparison are presented in **Table 6-2.**
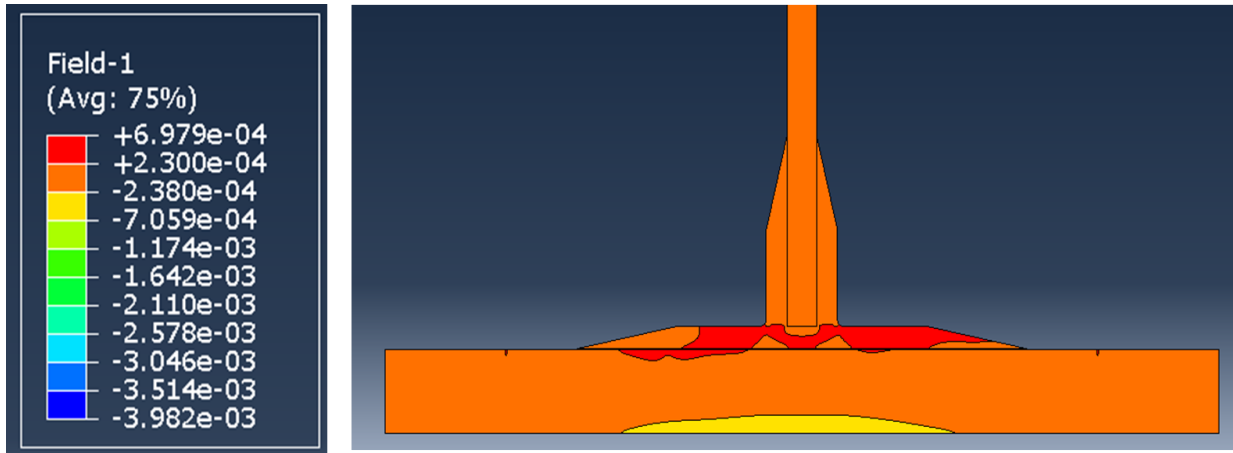
Figure 6-25. Numerical simulation on pi-joint with side-delamination at 1.9 kN load.

Table 6-2. Specimen C-2 Quantitative Data Comparison.

$\Delta\varepsilon_{exp}$	1 x 597 $\mu\varepsilon = 0.597$ x 10^{-3} mm/mm
$\Delta\varepsilon_{sim}$	0.392×10^{-3} mm/mm
%difference	34.30%
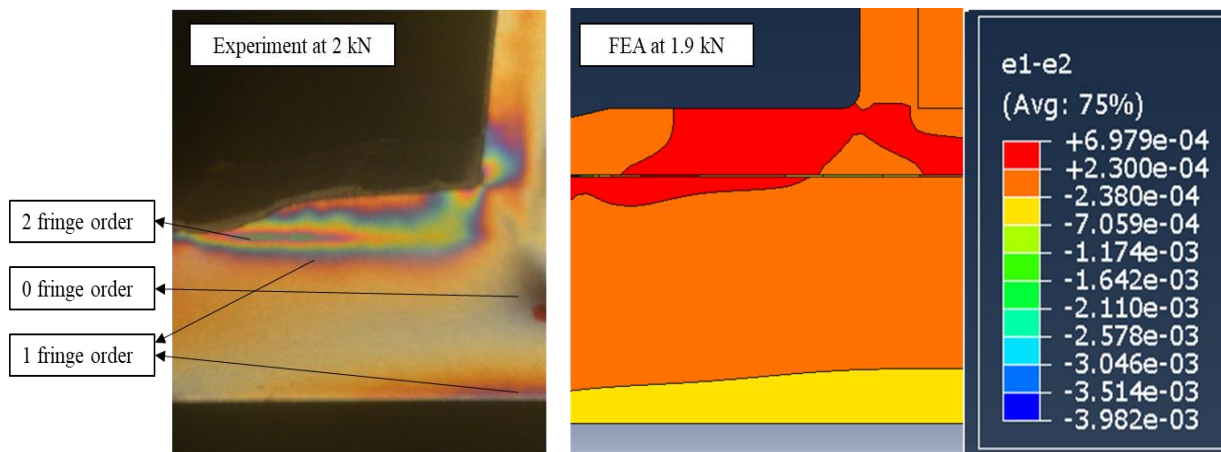
Figure 6-26. Comparison of isochromatic fringe pattern and finite element analysis result on a side-delamination aluminum pi-joint, specimen C-2.

The region on the bottom center of the pi-joint was arbitrarily chosen for data comparison because poor modeling of the effects of the actual delamination created was suspected, while qualitative study suggested that the simulation was nearer reality in the bottom where bending predominates. The quantiative comparison shows only fair agreement of photoelasticity results and finite element analysis. The difference of 34.3% is much larger than that found for the healthy/ pristine pi-joint. It appears that the indadequate simulation of the effects of the delamination resulted in a model that is stiffer than physically possible, and the resulting strains are, therefore, significantly smaller. The relative minor degree of asymmetry observed in the numerical solution supports this idea. Alternatively, it is possible that the photoelasticity specimen had some fault in the cohesive zone adjacent to the delamination, thereby making the specimen more compliant.

Chapter 7 Conclusion and Future Work

7.1 Conclusion

Six specimens of a multi-material pi-joint consisting of aluminum substrates and a carbon fiber preform were successfully manufactured using the vacuum assisted resin transfer molding technique (VARTM). Pristine joints and joints with middle and edge delaminations were tested experimentally and modeled numerically. Prior to the testing and analysis of the pi-joints, the methodologies were developed and refined to some extent by testing a structural steel T-joint. Then, one pi-joint specimen of each type was tested in pull-out to establish the failure load and the load-displacement profile. Subsequently, one specimen of each type was examined to determine the distribution of difference of principal strains for comparison with the simulations.

The distributions of difference of principal strains of the pi-joints was determined experimentally using the photoelasticity coating method. Isochromatic fringe patterns yielded by the method offer visualizations of the strain distribution in these complex joints during web pull-out. Only fringe color interpretation was used to determine isochromatic fringe orders in the photoelasticity tests.

The numerical simulations were accomplished through finite element modeling using ABAQUS®. The preform to substrate bond lines were modeled only as a single layer of elements. Hence, the number of elements present in the adhesive layer were limited, but still able to model failure of the dissimilar material T-joint.

The results of the load tests as well as the simulations and the photoelasticity studies of the pi-joints can be summarized as follows:

1. The failure pull-out load for a typical pi-joint with no defects was at 18 kN load, and the load-displacement behavior agreed well with that determined from the simulation. Ultimate failure was at the interface between the base and the web and preform. Results from photoelasticity and simulation at 5 kN load, chosen to be well within the linear

response region, were compared for the region at the middle of the bottom of the base where bending predominates. The principal strain differences drawn from experiment and analysis agreed to within 5.86 %.

2. The failure load for the joint having an embedded delamination in the middle part of the preform-base interface was predicted by the simulation to be 14 kN or 77% of the pristine pi-joint strength. The failure load found from the pull-out test was only 2 kN. Examination of the failure surface showed that bonding between the preform and the base was very poor, probably as a result of inadequate specimen preparation or faulty resin infusion owing to a vacuum leak during VARTM. The matching photoelasticity specimen was observed at very small load. The fringe pattern showed considerable lack of symmetry, suggesting that this specimen, too, had faulty bond line cohesion. No comparison with the numerical simulation was carried out for this case.

3. When the same delamination was installed on the side of the preform-base interface, it was found that it caused even more strength loss, with the failure pull-out load being measured at 11 kN or 61 % of the flawless pi-joint failure load. Numerical simulation built using cohesive elements on ABAQUS © were able to capture the load distribution along the complex joint. Qualitatively, the strain distribution from the finite element analysis were much more symmetric than that found from the photoelasticity of this specimen. This difference suggests that the model was much stiffer than the specimen, implying that the simulation of the delamination was not adequate or else the specimen contained some bonding defects adjacent to the delamination. These ideas are supported by the fact that the maximum difference of principal strains calculated for the center-bottom exceeded those found from photoelasticity by about 34%.

4. All in all, the photoelasticity coating method was reestablished to measure strain distribution on the novel multi-material pi-joint and served well as an assessment tool to validate the numerical simulations built to design the joints.

7.2 Future Work

Although this work demonstrates that the classic photoelasticity coating method is able to characterize the complex behavior of dissimilar composite pi-joints, further work is required to generate higher confidence in the results of both experiment and simulation. Future work regarding photoelasticity application on an aluminum pi-joints consist of three main parts:

1. Manufacturing.

The process of pi-joint manufacturing could benefit by adding a surface preparation step such as etching of the metal substrate before resin infusion. There are many studies that show that metal to composite bonding fundamentally relies on the interaction between the adhesive and the bonded surface. Adhesive bond quality of the metal-to-composite will be stronger and more consistent with implementation of this improvement.

2. Experimental Photoelastic Coating Method

In this work, validation of the strain in the isochromatic fringe coating was based on only one value that was that was located in the base of the pi-joint. Furthermore, only fringe counting by matching fringe colors with the standard chart was used, thus limiting both sensitivity and accuracy. Future work will benefit from using an image processing technique that is able to directly compute and map all strain values over the extent of the specimen. After all, whole-field analysis is one of the several advantages of photoelsticity. Such automation is readily available through the Tardy compensation method, RGB photoelasticity, or phase-shifting photoelasticity. Digital image

76

analysis of the entire isochromatic fringe pattern facilitates easier and faster comparisons with the strain maps derived from simulations.

3. Numerical Simulation

Simulation in this work was designed using a limited number of elements and nodes. For example, the adhesive in the preform-base interface was modeled using only one layer of adhesive elements. Such a model does not allow actual cohesive failure, where the mating surfaces retained resin from the infusion. Adding more adhesive layer elements would improve the simulation results to more closely match physical reality.

REFERENCES

REFERENCES

[1] S. D. Thoppul, J. Finegan, and R. F. Gibson, "Mechanics of mechanically fastened joints in polymer–matrix composite structures – A review," *Composites Science and Technology*, vol. 69, no. 3, pp. 301–329, 2009.

[2] A. Kesavan, M. Deivasigamani, S. John, and I. Herszberg, "Damage detection in T-joint composite structures," *Composite Structures*, vol. 75, no. 1–4, pp. 313–320, Sep. 2006.

[3] K. I. Tserpes, R. Ruzek, and S. Pantelakis, "Strength of Pi shaped non-crimp fabric adhesively bonded joints," *Plastics, Rubber and Composites*, vol. 41, no. 2, pp. 100–106, Mar. 2012.

[4] C. Sebastian, M. Haq, and E. Patterson, "Analysis of a Composite Pi/T-Joint Using an FE Model and DIC," in *Joining Technologies for Composites and Dissimilar Materials, Volume 10*, Springer, Cham, 2017, pp. 11–19.

[5] D. C. Álvarez, M. Haq, J. de D. C. Álvarez, and E. A. Patterson, "Photoelastic Testing and FE Analysis of T-Stub Model," in *Imaging Methods for Novel Materials and Challenging Applications, Volume 3*, H. Jin, C. Sciammarella, C. Furlong, and S. Yoshida, Eds. New York, NY: Springer New York, 2013, pp. 359–367.

[6] L. R. O. de Lima, J. L. de F. Freire, P. C. G. da S. Vellasco, S. A. L. de Andrade, and J. G. S. da Silva, "Structural assessment of minor axis steel joints using photoelasticity and finite elements," *Journal of Constructional Steel Research*, vol. 65, no. 2, pp. 466–478, Feb. 2009.

[7] D. W. Fritz, "The Photoelastic Coating Method Applied to the Stress Analysis of Wood," Oregon State University, 1967.

[8] G. Gardiner, "Wind blades: Pi preforms increase shear web failure load." [Online]. Available: https://www.compositesworld.com/articles/wind-blades-pi-preforms-increase-shear-web-failure-load-. [Accessed: 24-Apr-2018].

[9] US Department of Energy, "WORKSHOP REPORT:Light-Duty Vehicles Technical Requirements and Gaps for Lightweight and Propulsion Materials," *FINAL REPORT*, p. 56, Feb. 2013.

[10] H. C. H. Li, F. Dharmawan, I. Herszberg, and S. John, "Fracture behaviour of composite maritime T-joints," *Composite Structures*, vol. 75, no. 1–4, pp. 339–350, Sep. 2006.

[11] J. M. Dulieu-Smith, S. Quinn, R. A. Shenoi, P. J. C. L. Read, and S. S. J. Moy, "Thermoelastic stress analysis of a GRP tee joint," *Applied Composite Materials*, vol. 4, no. 5, pp. 283–303, Sep. 1997.

[12] J. D. Russell, "Composites Affordability Initiative (CAI) Overview," *2006 ASIP Conference San Antonio TX*, p. 20.

[13] J. E. Higgins and L. Pelham, "Application of Pi Preform Composite Joints in Fabrication of NASA Composite Crew Module Demonstration Structure (Abstract)," p. 5.

[14] D. Brewster, "On the effects of simple pressure in producing that species of crystallization which forms two oppositely polarised images, and exhibits the complementary colours by polarised light," *Philosophical Transactions of the Royal Society of London*, vol. 105, pp. 60–64, 1815.

[15] E. G. Coker and L. N. G. Filon, *A treatise on photo-elasticity*. Cambridge : Cambridge University Press, 1931.

[16] M. M. Leven (Ed), *"Photoelasticity"The Selected Scientific Papers of M. M. Frocht*. Pergamon Press, 1969.

[17] D. Post and F. Zandman, "Accuracy of birefringent-coating method for coatings of arbitrary thickness: Authors endeavor to develop and verify rational concepts of the behavior of birefringent coatings, as a step toward general understanding of the factors that control accuracy of method," *Experimental Mechanics*, vol. 1, no. 1, pp. 21–32, Jan. 1961.

[18] F. Zandman, S. S. Redner, and E. I. Riegner, "Reinforcing effect of birefringent coatings: Strains derived directly from birefringence data are related to the surface strains that would have developed if the part had not been coated," *Experimental Mechanics*, vol. 2, no. 2, pp. 55–64, Feb. 1962.

[19] J. K. Meisenheimer, "An investigation of the application of photoelastic coatings to soil studies," p. 76.

[20] H. Driscoll, H. Koerger, T. Senior, and S. Haake, "The use of photoelasticity to identify surface shear stresses during running," *Procedia Engineering*, vol. 2, no. 2, pp. 3047–3052, Jun. 2010.

[21] G. Cloud, *Optical Methods of Engineering Analysis*. Cambridge University Press, 1998.

[22] K. Ramesh, *Digital Photoelasticity: Advanced Techniques and Applications*. Springer Science & Business Media, 2012.

[23] E. A. Patterson, "Digital Photoelasticity: Principles, Practice and Potential," *Strain*, vol. 38, no. 1, pp. 27–39, Feb. 2002.

[24] G. Cloud, "Optical Methods in Experimental Mechanics.: Part 31: Photoelasticity III—Theory," *Experimental Techniques*, vol. 32, no. 2, pp. 11–15, Mar. 2008.

[25] G. Cloud, "Optical Methods in Experimental Mechanics: Part 42: Photoelasticity XIV-Reflection Photoelasticity," *Experimental Techniques*, vol. 34, no. 4, pp. 15–19, Jul. 2010.

[26] C. P. Fernandes, P.-O. J. Glantz, S. A. Svensson, and A. Bergmark, "Reflection photoelasticity: a new method for studies of clinical mechanics in prosthetic dentistry," *Dental Materials*, p. 12, 2003.

[27] F. Caputo and G. Giudice, "Photoelastic coating method approach to the study of stress distribution in composite materials," *Fibre Science and Technology*, vol. 18, no. 4, pp. 255–264, Jan. 1983.

[28] Micro-Measurements, "Tech Note TN-704-2 'How to Select Photoelastic Coatings.'" 04-Aug-2015.

[29] C. Adams and J. G. Beese, "The reinforcing effect of birefringent coatings when applied to plastically deformed structures," *Journal of Physics D: Applied Physics*, vol. 8, no. 9, pp. 1084–1091, Jun. 1975.

[30] Micro-Measurements, "Application Note B-223 'Instructions for Bonding Flat and Contoured PhotoStress® Sheets.'" 07-Mar-2017.

[31] "Abaqus Analysis User's Manual (6.10)." [Online]. Available: https://www.sharcnet.ca/Software/Abaqus610/Documentation/docs/v6.10/books/usb/default.htm?startat=pt05ch21s02abm42.html. [Accessed: 06-Mar-2018].

[32] E. J. Barbero, *Finite element analysis of composite materials using Abaqus*. Boca Raton, FL: CRC Press,Taylor & Francis Group, 2013.

[33] R. B. Bucinell, Symposium on Composites: Fatigue and Fracture, American Society for Testing and Materials, and American Society for Testing and Materials, Eds., *Composite materials: fatigue and fracture, seventh volume ; [papers presented at the Seventh Symposium on Composites: Fatigue and Fracture, held in St. Louis, Missouri, on 7 - 8 May 1997]*. West Conshohocken, Pa: ASTM, 1998.

[34] T. C. Truong, M. Vettori, S. Lomov, and I. Verpoest, "Carbon composites based on multi-axial multi-ply stitched preforms. Part 4. Mechanical properties of composites and damage observation," *Composites Part A: Applied Science and Manufacturing*, vol. 36, no. 9, pp. 1207–1221, Sep. 2005.

[35] Micro-Measurements, "Introduction to Stress Analysis by the PhotoStress® Method, Technical Note TN-702-2," Jun. 2011.